

Vertically Integrated Dual-memtransistor Enabled Reconfigurable Heterosynaptic Sensorimotor Networks and In-memory Neuromorphic Computing

Srilagna Sahoo,[†] Abin Varghese,[‡] Aniket Sadashiva,[†] Mayank Goyal,[†] Jayatika
Sakhuja,[†] Debanjan Bhowmik,[†] and Saurabh Lodha^{*,†,¶}

[†]*Department of Electrical Engineering, Indian Institute of Technology Bombay, Mumbai
400076, India*

[‡]*Department of Engineering, King's College London, London WC2R 2LS, UK*

[¶]<https://orcid.org/0000-0002-0690-3169>

E-mail: slodha@ee.iitb.ac.in

Keywords

2D materials, vdW, Heterostructure, Multiterminal, Ferroelectric, In₂Se₃, MoS₂, Homosynaptic and Heterosynaptic plasticity, Synaptic interactions, Synaptic cooperation, Synaptic competition, Logic gates

Abstract

Neuromorphic in-memory computing requires area-efficient architecture for seamless and low latency parallel processing of large volumes of data. Here, we report a compact, vertically integrated/stratified field-effect transistor (VSFET) consisting of

a 2D non-ferroelectric MoS₂ FET channel stacked on a 2D ferroelectric In₂Se₃ FET channel. Electrostatic coupling between the ferroelectric and non-ferroelectric semiconducting channels results in hysteretic transfer and output characteristics of both FETs. The gate-controlled MoS₂ memtransistor is shown to emulate homosynaptic plasticity behavior with low nonlinearity, low epoch, and high accuracy supervised (ANN - artificial neural network) and unsupervised (SNN - spiking neural network) on-chip learning. Further, simultaneous measurements of the MoS₂ and In₂Se₃ transistor synapses help realize complex heterosynaptic cooperation and competition behaviors. These are shown to mimic advanced sensorimotor neural network-controlled gill withdrawal reflex sensitization and habituation of a sea mollusk (*Aplysia*) with ultra-low power consumption. Finally, we show logic reconfigurability of the VSFET to realize Boolean gates thereby adding significant design flexibility for advanced computing technologies.

Introduction

In today's data-intensive world, research in future computing paradigms is pursuing alternate paths compared to the traditional scaling of complementary metal oxide semiconductor (CMOS) transistor technology. Applications such as artificial intelligence, challenged by the von Neumann bottleneck, demand high performance as well as energy- and area-efficient computing devices with logic-in-memory functionality. This can be addressed by brain-inspired neuromorphic computing devices that offer in-memory computing with parallel processing capability along with low energy consumption and latency.^[1] Their fundamental components are neurons (responsible for processing) that are connected to each other by synapses (responsible for storage) to form a neural network (NN). However, the challenges in realizing neuromorphic devices lie in material limitations that hinder the effective integration of memory and logic and, secondly, architecture that is both energy- and area-efficient.

Ferroelectric field effect transistors (Fe-FETs) offer one such option of integrating logic and memory in a single, area-efficient device.^[2] Conventional Fe-FETs involve stacking the

semiconducting channel layer with an out-of-plane ferroelectric dielectric or polymer as gate dielectric to demonstrate a modulated memtransistor for synapses and logic circuits.^[3–6] However, conventional bulk ferroelectric dielectrics (BaTiO₃, Pb(Zr, Ti)O₃, BiFeO₃) suffer from degradation of ferroelectric properties with thickness scaling, charge trapping, and poor interfaces.^[7] In recent years, two-dimensional (2D) van der Waals (vdW) ferroelectrics have drawn attention because of their room temperature atomic level ferroelectricity, a dangling bond-free surface and high-quality heterointerfaces due to the absence of lattice mismatch with other materials.^[8–12] CuInP₂S₆ (CIPS) is one such 2D vdW ferroelectric dielectric that shows out-of-plane (OOP) ferroelectricity in ultra-thin flakes.^[8,9,13] Unlike conventional insulating ferroelectrics, 2D vdW ferroelectrics can also be semiconducting in nature. This offers an additional degree of freedom in the design of ferroelectric semiconductor (FeS) FETs (FeS-FETs) for logic-in-memory functionality.^[14,15] Ferroelectric 2D vdW semiconductors such as SnSe,^[16] and SnS^[17,18] show in-plane (IP) ferroelectric polarization.^[10] In₂Se₃ on the other hand shows both IP and OOP ferroelectricity, which makes it suitable for multi-directional conductivity control device architectures.^[19,20] Several memory device and neural network designs using In₂Se₃ as a semiconductor channel or a ferroelectric gate have been reported in conjunction with CIPS^[8], MoS₂^[21], and hBN^[22,23]. However, reported structures are either area-inefficient (lateral or multi-device architecture), and/or they do not simultaneously exploit their semiconducting and correlated IP and OOP ferroelectric polarization properties.

In this work, we demonstrate a compact, vertically stacked heterostructure FET where the 2D vdW semiconductor (S) MoS₂ is stacked upon ferroelectric semiconductor (FeS) In₂Se₃ on gate insulator (I) hBN aligned over the metal (M) gate to form a MIFeSS structure in a top-down approach. Lateral electrodes are placed on both semiconductors such that they can be readily accessed simultaneously. The FeS In₂Se₃ is stacked on top of the gate electrode and beneath the MoS₂ to gain maximum control on its polarization and mobile charge, while its OOP polarization can be leveraged to tune MoS₂ conduction. This densely

packed vertical stratified field-effect transistor (VSFET) architecture utilizing a non-FeS/FeS heterostructure harnesses not only the semiconducting properties of each layer but also the interface FeS-S coupling between them.

This work consists of three parts. The first part utilizes the electrostatic coupling between MoS₂ (S) and In₂Se₃ (FeS) to demonstrate hysteretic behavior in transfer (drain current vs. gate voltage: $I_D - V_G$) and output (drain current vs. drain voltage: $I_D - V_D$) characteristics of the MoS₂ FET. The gate-modulated MoS₂ memtransistor is shown to emulate biological input-specific Hebbian homosynaptic plasticity behavior with low nonlinearity, and high accuracy supervised (ANN - artificial neural network) and unsupervised (SNN - spiking neural network) on-chip learning. In the second part, we demonstrate advanced biomimetic heterosynaptic cooperation and competition between the two simultaneously measured MoS₂ and In₂Se₃ memtransistors representing two distinct but coupled synapses. This heterosynaptic behavior is shown to replicate the highly developed sensorimotor NN governing the gill reflexes of a sea mollusk. Finally, the realization of two-input Boolean logic gates comprehensively shows the area-efficient, logic, and multi-memory reconfigurability of the VSFET architecture.

Results

Device Architecture: A three-dimensional (3D) schematic of the VSFET stack consisting of Au (bottom gate)/hBN (dielectric)/n-type In₂Se₃ (FeS)/n-type MoS₂ (top S) is shown in Figure 1a. 2D cross-section of the MoS₂/In₂Se₃ VSFET that shows heterostructure stacking of two individual FET channels (top MoS₂: HT-MoS₂ and bottom In₂Se₃: HB-In₂Se₃) is depicted in Figure 1b, enabling 2D vdW FeS-S coupling that can modulate the HT-MoS₂ electron conduction (Figure 1c). The bottom metal gate was patterned on a 285 nm SiO₂/Si substrate using electron beam (e-beam) lithography and metal deposition (4 nm Ti/30 nm Au) by sputtering. A thick (74.4 nm) hBN flake was then transferred onto the Ti/Au gate

electrode. Next, a thick (43.2 nm) In_2Se_3 flake was transferred onto the hBN and metal gate overlap area. Finally, a thin (4.5 nm) MoS_2 flake was transferred on top of the In_2Se_3 flake transversely such that some part of MoS_2 forms a heterojunction with the In_2Se_3 flake, and some part gets transferred directly onto the hBN flake to form a control MoS_2 (C- MoS_2) FET (Figure S1a) that works as a control device without In_2Se_3 . Likewise, the exposed part of In_2Se_3 on the hBN flake forms the control In_2Se_3 (C- In_2Se_3) FET that serves as the other control device without MoS_2 (Figure S1a). Following all the flake transfers, the source/drain (S/D) electrodes were e-beam patterned and metallized (4 nm Ti/100 nm Au) by sputtering. A false color optical micrograph of the fabricated device is shown in Figure 1d. Thicknesses of the hBN, In_2Se_3 , and MoS_2 layers characterized by atomic force microscopy (AFM) scans are reported in Figure 1e.

Raman scattering peaks of C- MoS_2 were observed at 382.4 cm^{-1} and 406.3 cm^{-1} corresponding to E_{2g} and A_{1g} phonon modes respectively (Figure 1f).^[24,25] A difference of 24 cm^{-1} between them indicates ≥ 4 -layer thickness of MoS_2 , but confirmed to be ~ 6 -layer thick based on AFM height profile (Figure 1e).^[26,27] The four Raman peaks observed at 90.1 cm^{-1} , 102.6 cm^{-1} , 180.4 cm^{-1} , and 193.2 cm^{-1} indicate the typical E, $A_1(\text{LO}+\text{TO})$, $A_1(\text{LO})$, and $A_1(\text{TO})$ phonon modes of α -phase In_2Se_3 respectively (Figure 1f).^[28,29] The Raman peak at 90.1 cm^{-1} indicates the hexagonal symmetry of α - In_2Se_3 .^[30] The presence of $A_1(\text{LO})$ and $A_1(\text{TO})$ phonon modes due to LO-TO splitting indicates the lack of inversion symmetry, making α - In_2Se_3 ferroelectric.^[29] Signature peaks of both materials are also present in the VSFET overlap region. α - In_2Se_3 exhibits correlated IP and OOP polarization^[20], wherein OOP polarization is due to a breaking of centrosymmetry due to the asymmetric position of the middle Se layer in the 5-layer (Se-In-Se-In-Se) structure of In_2Se_3 .^[19] Polarization switching in the In_2Se_3 layer was characterized by piezoresponse force microscopy (PFM) (Figures S1b-c). A butterfly-like amplitude vs. voltage loop and a phase shift of 180° were obtained, indicating ferroelectric switching in In_2Se_3 .^[31,32]

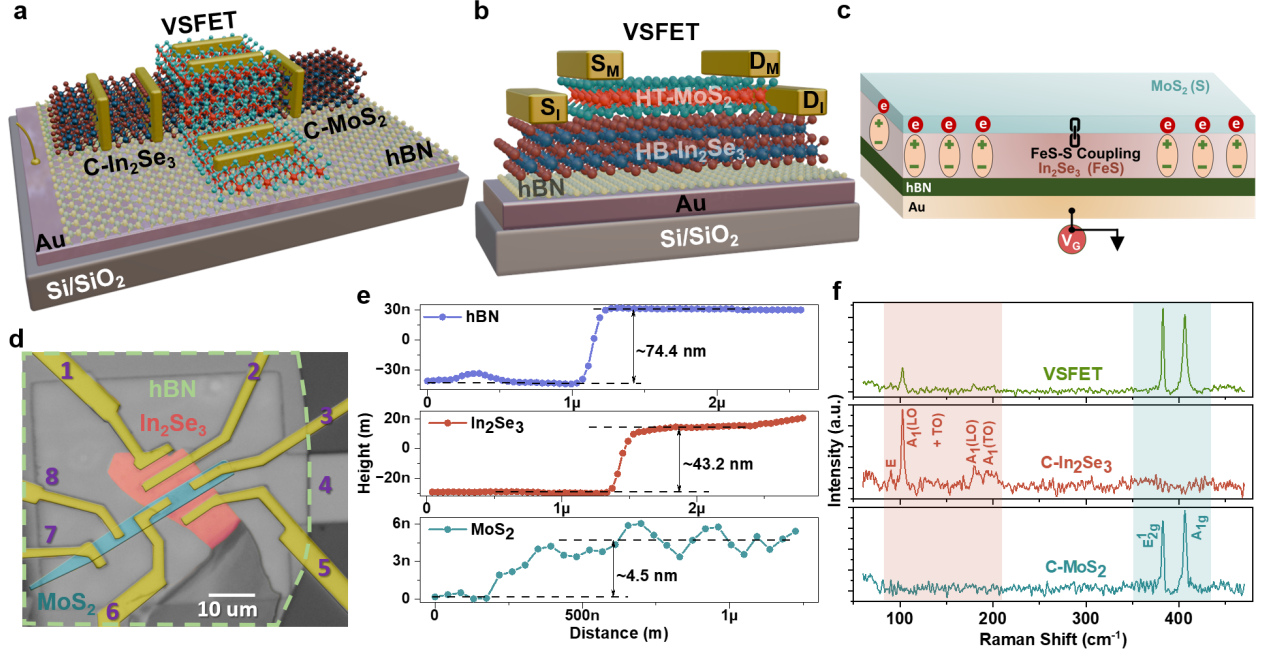


Figure 1: Device structure and Raman spectra. (a) 3D schematic of MoS₂ and In₂Se₃ vertical stratified field-effect transistor (VVFET) with hBN as the gate dielectric. (b) 2D cross-section of MoS₂/In₂Se₃ VVFET. (c) Pictorial representation of 2D ferroelectric and non-ferroelectric semiconductor coupling that modulates HT-MoS₂ electron current. (d) False color optical microscope image of the fabricated vdW heterostructure VVFET on Au/SiO₂/p⁺ Si substrate. Dashed line indicates the boundary of the hBN flake. (e) Thickness profiles of hBN, In₂Se₃, and MoS₂ characterized by atomic force microscopy. (f) Raman spectra acquired from C-MoS₂, C-In₂Se₃, and the MoS₂/In₂Se₃ heterojunction regions.

Electrical Characterization: Transfer characteristics of both the MoS₂ (C-MoS₂ and HT-MoS₂) FETs show n-type behavior and clockwise hysteresis with gate bias sweeps from $-5 \text{ V} \rightleftharpoons 5 \text{ V}$ under $V_D = 1 \text{ V}$ (Figure 2a). However, HT-MoS₂ FET shows significantly larger hysteresis because of the underlying ferroelectric In₂Se₃, compared to the C-MoS₂ FET. The C-MoS₂ FET shows an on-/off- current (I_{on}/I_{off}) ratio of 10^6 , whereas HT-MoS₂ FET shows a $3\times$ ratio. The low ratio is due to the extra ferroelectric capacitance (C_{FE}) from In₂Se₃ in series with the dielectric capacitance (C_{hBN}) in the HT-MoS₂ FET, resulting in poor gate modulation. Transfer curves with 0.5 V drain bias for HT-MoS₂ and C-MoS₂ FETs are shown in Figure S3a.

Further, to investigate the origin of hysteresis in the HT-MoS₂ FET, I_D was measured with maximum gate sweep voltage ($|V_{Gmax}|$) increasing from 1 V to 10 V (Figure 2b). The

hysteresis loop memory window (MW) expansion with increasing $|V_{Gmax}|$ is due to gate field-controlled gradual increase in ferroelectric polarization charge of the underlying In_2Se_3 layer. Here, MW refers to the maximum hysteresis window seen at a constant value of drain current. This indicates effective modulation of carrier transport in the MoS_2 channel due to ferroelectric coupling with In_2Se_3 .^[22] In contrast, increasing $|V_{Gmax}|$ does not increase the hysteresis window in the $I_D - V_G$ loops for the C- MoS_2 FET, as shown in Figure S2a. Progressive increase of the hysteresis window in the $I_D - V_G$ loops for C- In_2Se_3 and HB- In_2Se_3 FETs is shown in Figures S2b-c. Similar progressive increase in the hysteretic memory window at a lower 0.5 V drain bias is shown in Figures S3b-e for C- MoS_2 , HT- MoS_2 , C- In_2Se_3 , and HB- In_2Se_3 , respectively. The MW-to-sweep range (SR) ratio (MW/SR) of all four FETs versus $|V_{Gmax}|$ is shown in Figure 2c, indicating a monotonic increase in the MW/SR ratio for HT- MoS_2 with $|V_{Gmax}|$, like the In_2Se_3 FETs (C- and HB-), and unlike the C- MoS_2 FET. The MW/SR ratio measurements were repeated on two additional HT- MoS_2 FETs with similar results (Figure S2d). The MW/SR data of all four FETs for $V_D = 0.5$ V is shown in Figure S3f. Gate tunable output ($I_D - V_D$) characteristics of C- MoS_2 , HT- MoS_2 , C- In_2Se_3 , and HB- In_2Se_3 FETs are shown in Figure S4.

While the OOP polarization charge of HB- In_2Se_3 modulates HT- MoS_2 transfer characteristics, the IP polarization charge of HB- In_2Se_3 also modulates HT- MoS_2 output characteristics at 0 V gate bias (no OOP field, Figure 2d). Sweeping the drain bias along $0 \text{ V} \rightarrow +V_{Dmax} \rightarrow 0 \text{ V}$ and then $0 \text{ V} \rightarrow -V_{Dmax} \rightarrow 0 \text{ V}$, the output curve shows a hysteresis loop (directions are marked in black arrows) pinched at 0 V. These pinched hysteresis loops (PHLs) open up gradually from a closed state ($|V_{Dmax}| = 1 \text{ V}$) with increasing $|V_{Dmax}|$. This leads to the appearance of two distinct resistive states R_{High} and R_{Low} for higher $|V_{Dmax}|$ values, where $R = V_D/I_D$. The resistive switching behavior could be attributed to IP (lateral) ferroelectric domain propagation in HB- In_2Se_3 that affects the lateral transport characteristics in HT- MoS_2 through Schottky barrier modulation at the contacts. The resistance window opens up after the IP coercive voltage (V_{cip}) is reached. $1 \text{ V} < V_{cip} < 2 \text{ V}$ and beyond $|V_{Dmax}|$

≥ 2 V, the resistance ratio (RR): R_{High}/R_{Low} at a read drain bias voltage V_R , increases till $V_{Dmax} = -5$ V and saturates thereafter due to the saturation of In_2Se_3 IP polarization.^[33] The asymmetry observed in PHLs for $+V_{Dmax}$ and $-V_{Dmax}$ is likely due to the asymmetry in contact areas. The inset of Figure 2d shows pinched output hysteresis loops for $|V_{Dmax}| = 1 \text{ V} \rightarrow 4 \text{ V}$, indicating the gradual opening of the resistive window even at lower voltage ranges. However, the output curve of C-MoS₂ FET (Figure 2e) shows no such resistive window opening for $|V_{Dmax}| = 1 \text{ V} \rightarrow 4 \text{ V}$ (inset of Figure 2e). For $V_{Dmax} \geq -5$ V, a non-gradual hysteresis window opening can be seen, most likely due to a high electric field that can introduce defects (field-induced trap generation), resulting in a threshold voltage shift. The RRs for negative drain bias, shown in Figure 2f, are higher compared to positive drain bias. RRs, extracted at a fixed drain bias V_R , for three different gate biases versus $|V_{Dmax}|$, are shown for C-MoS₂ and HT-MoS₂ FETs. HT-MoS₂ has a higher RR than C-MoS₂ due to its HB- In_2Se_3 IP ferroelectric polarization modulated conductance. In summary, the intercorrelated IP-OOP polarization of In_2Se_3 can effectively tune both the trans- and output-conductance of HT-MoS₂.

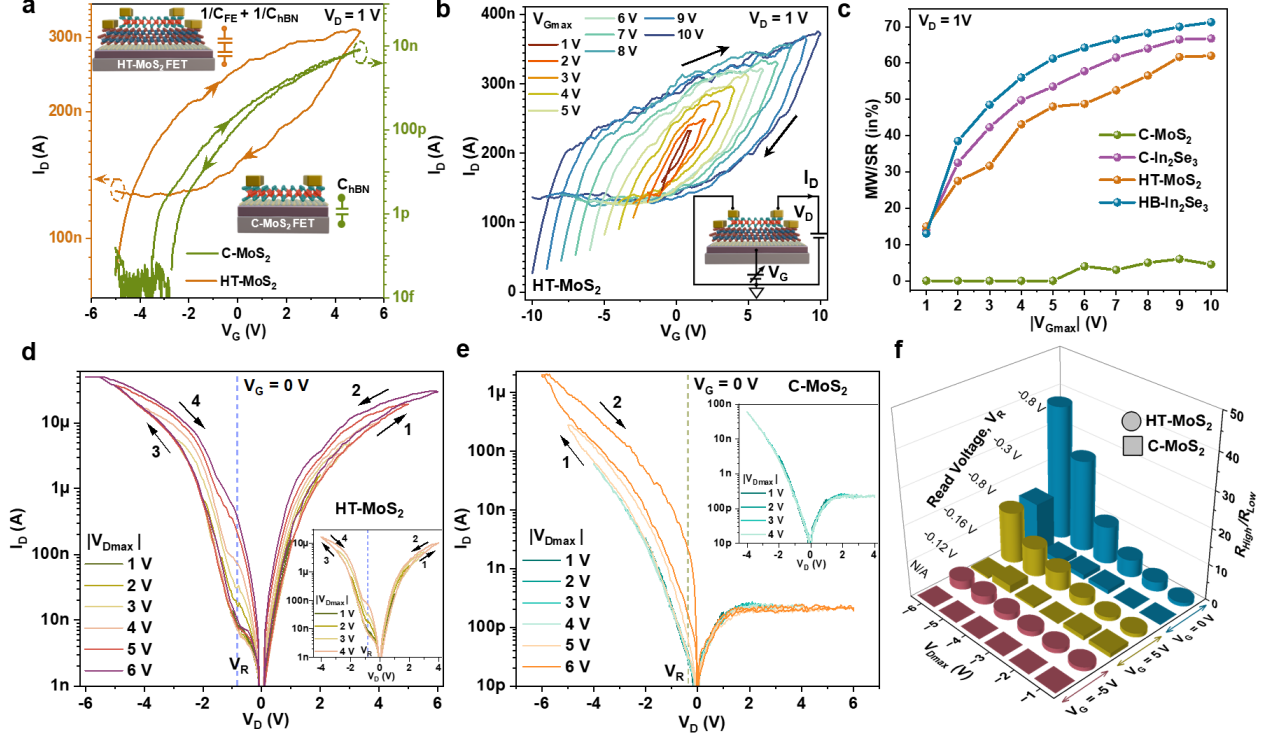


Figure 2: DC electrical characteristics of VSFET. (a) Comparison of transfer characteristics between C-MoS₂ and HT-MoS₂ FETs at $V_D = 1$ V showing notable hysteretic behavior in HT-MoS₂ in contrast to C-MoS₂. (b) $I_D - V_G$ characteristics of HT-MoS₂ FET under different gate bias sweeps. (c) MW/SR ratios of C-MoS₂, C-In₂Se₃, HT-MoS₂, and HB-In₂Se₃ FETs as a function of maximum gate bias sweep range. (d) Pinched output hysteresis loops ($I_D - V_D$) of HT-MoS₂ under different drain bias sweep ranges. The inset shows pinched output hysteresis loops for $|V_{Dmax}| = 1$ V \rightarrow 4 V, indicating the gradual opening of the resistive window at lower voltages. However, (e) output curves of C-MoS₂ FET show no such resistive window opening for $|V_{Dmax}| = 1$ V \rightarrow 4 V (inset). For $V_{Dmax} \geq -5$ V, a non-gradual resistive window opening can be seen likely due to higher V_D . (f) The resistance ratio versus V_{Dmax} for C-MoS₂ and HT-MoS₂ FETs for three different gate voltages (0 V, 5 V, -5 V).

Device Physics: The clockwise hysteretic behavior in the transfer characteristics of HT-MoS₂ (Figure 2a) can be explained using the local gate field and ferroelectric polarization in In₂Se₃ as shown in Figure 3 through energy band diagrams (EBDs) of the Au/hBN/In₂Se₃/MoS₂ stack at four representative V_G conditions. EBDs of each individual material used in the heterostructure before contact^[24,25,34-38] and at equilibrium after contact are described in supporting information in Figure S5a-b. Equilibrium EBD (Figure S5b) indicates an accumulated MoS₂ interface with In₂Se₃ consistent with a conducting MoS₂ channel at $V_G = 0$ V (transfer curve in Figure 3a).

At $-V_{Gmax}$ of -10 V (point 1 (Figure S5c) on $I_D - V_G$ curve), the electric field across the 43 nm thick In_2Se_3 layer is higher than its coercive field, resulting in a fully polarized In_2Se_3 layer with positive polarization charge at the hBN/ In_2Se_3 interface and negative fixed polarization charge at the $\text{In}_2\text{Se}_3/\text{MoS}_2$ interface. The series combination of hBN and In_2Se_3 capacitances leads to a lower effective capacitance and poor modulation of the drain current, which stays high, and HT-MoS₂ does not turn off entirely. However, the negative polarization charge near the $\text{In}_2\text{Se}_3/\text{MoS}_2$ interface reduces electron concentration in the MoS₂ channel and the off-current is lower than what it would have been without the OOP polarization in In_2Se_3 .

Likewise, at $+V_{Gmax}$ of +10 V (point 3 (Figure S5c) on $I_D - V_G$ curve), the polarization field in the In_2Se_3 layer flips such that we have negative charge at the hBN/ In_2Se_3 interface and positive at the $\text{In}_2\text{Se}_3/\text{MoS}_2$ interface. The positive polarization charge near the $\text{In}_2\text{Se}_3/\text{MoS}_2$ interface increases electron concentration in the MoS₂ channel and the on-current is higher than what it would have been without the OOP polarization in In_2Se_3 .

However, the origin of the hysteresis is due to the difference in the electrostatics at points 2 and 4 (EBDs in Figure 3b-c) of the $I_D - V_G$ curve. Here, EBDs for point 2 and point 4 illustrate the change in electrostatics, spatial electric field, and charge distribution corresponding to a change in $|V_{Gmax}|$ from 6 V (low field, red) to 10 V (high field, blue). At point 2 ($V_G = 0^+$, forward V_G sweep) for high $|V_{Gmax}| = 10$ V, the In_2Se_3 layer is partially (upward) polarized but with a more accumulated MoS₂ channel (higher current than without polarization), similar to the electrostatics at point 3 (Figure S5c). Conversely, at point 4 ($V_G = 0^-$, reverse V_G sweep) for high $|V_{Gmax}| = 10$ V, the In_2Se_3 is partially (downward) polarized but with a less accumulated MoS₂ channel (lower current than without polarization), similar to the electrostatics at point 1 (Figure S5c). The higher on-current and lower off-currents at points 2 and 4, compared to the no-polarization case, open up a hysteresis memory window.

Since the partial polarization strengths at points 2 and 4 depend on the maximum gate field values ($|V_{Gmax}|$) and the polarization strengths at points 1 and 3, the MW is a function

of applied $|V_{Gmax}|$. The strengths of the polarization field, polarization bound charge and their position change with an increase in $|V_{Gmax}|$ from 6 V to 10 V, thereby changing the electron charge density (current) in the MoS₂ channel at point 2 and 4. The resulting memory window expansion with increasing $|V_{Gmax}|$ can be seen in the transfer curves (Figure 3).

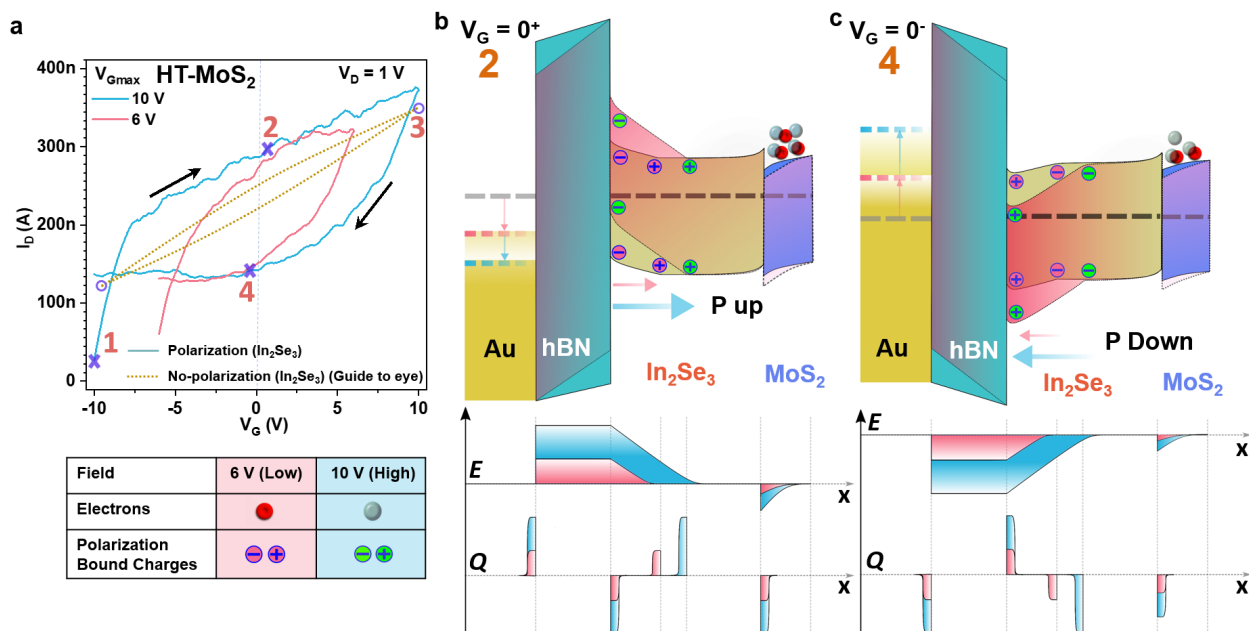


Figure 3: Device physics for $|V_{Gmax}|$ dependent $I_D - V_G$ hysteresis in HT-MoS₂ FET. (a) The transfer curve of HT-MoS₂ FET on the left has four marked points, 1, 2, 3, and 4, representing four operating points of the device in a clockwise direction for $|V_{Gmax}| = 10$ V. Energy band diagrams for (b) point 2 and (c) point 4 illustrate the change in electrostatics, spatial electric field, and charge distribution corresponding to a change in $|V_{Gmax}| = 6$ V (red) \rightarrow 10 V (blue). Point 2 (point 4) indicates a low positive (negative) gate field induced weak upward (downward) partial In₂Se₃ polarization and stronger (weaker) MoS₂ accumulation than without polarization. The higher (point 2) and lower (point 4) MoS₂ currents vs the no-polarization case open up a hysteresis memory window.

Homosynaptic Plasticity and Neuromorphic In-Memory Computing: Conductance modulation in HT-MoS₂ FET through gate-controlled ferroelectric polarization of the HB-In₂Se₃ layer can be leveraged for synapse functionality. Figure 4a illustrates a biological synapse and a corresponding electrical biasing scheme for HT-MoS₂ FET where the gate terminal serves as the presynaptic axon end, the source terminal serves as the starting point of the synaptic cleft, and the drain terminal mimics the postsynaptic end that collects the post-

synaptic current. Figure S6a (S6b) shows the excitatory (inhibitory) post-synaptic current (PSC) response for increasing negative (positive) amplitude pulses applied at the gate, due to the modulation in partial polarization consistent with the multi- $|V_{Gmax}|$ sweeps.^[31] Figures S6c and d show the same for different pulse widths. Figure S6e shows the paired-pulse facilitation data for varying pulse separation times, as illustrated in Figure S6f.

Potentiation (P, increase in synaptic strength) and depression (D, decrease in synaptic strength) are two key synaptic plasticity behaviors that help in learning and developing varied functionalities in neural circuits. Figure 4b shows the P/D behavior of the HT-MoS₂ synapse while applying 50 (50) incremental pulses (width = 100 ms, interval = 20 ms) in the negative (positive) direction from -0.1 V to -5 V (0.1 V to 5 V) with a step size of 0.1 V. During potentiation, the synapse conductance changed from 37.4 nS to 102 nS with non-linearity factor $\alpha_p = 1.74$. Likewise, during the depression, it changed from 100 nS down to 39.5 nS over 50 pulses with a non-linearity factor $\alpha_d = -0.07$. The different nonlinear rates for P and D result in an asymmetry factor ($\alpha_p - \alpha_d$) of 1.81 (see details in supporting information 7). Figure S8a shows multiple cycles of P/D data using this pulse scheme, whereas S8b and S8c show the P/D data for constant amplitude and varying pulse width schemes, respectively. The nonlinearity parameters for all the pulse schemes are tabulated in Table 1, supporting information 8.

Next, the P/D parameters extracted from Figure 4b were used to model the hardware implementation of a NN circuit utilizing MoS₂/In₂Se₃ vdW VSFET arrays in crossbar architecture, as shown in Figure 4c. A single cell of the crossbar matrix consists of two distinct memtransistors: 1) HT-MoS₂ FET at the top and 2) HB-In₂Se₃ FET at the bottom. Interestingly, the conductance levels of the two FETs are coupled owing to a common gate terminal. This coupling enables multiple additional functionalities, which will be discussed later. Here, the coupled gate terminal functions as the word line (WL), while the drain terminal of each HT-MoS₂ FET connects to the bit line (BL). The source terminal of each HT-MoS₂ FET is connected to the ground (GND), and V_{DD} serves as the supply voltage. Supervised learning

accuracy numbers using a non-spiking multilayer perceptron neural network (MLP), or fully connected neural network (FCNN), were evaluated for digit classification, as shown in Figure 4d. The three-layer MLP contains 784 input neurons in the first layer, 150 hidden neurons in the second layer, and 10 output neurons in the third layer (Figure 4d). A 28x28 pixel image from the MNIST dataset is shown in Figure 4d; it was given as input for the classification task. Each image pixel corresponds to one input neuron in the first layer.

For the learning accuracy evaluation, a back-propagation algorithm was used to update the synaptic weights at any iteration, limited to 1-step of potentiation or depression, consistent with the pulsing scheme. This 1-step or 1-bit weight update makes the crossbar array and peripheral circuit design simpler. Tanh and softmax neuronal activation functions were used for the hidden and output layers, respectively. Conductance non-linearity was considered as a non-ideal parameter during the MLP training. More details of the neural network design and the training algorithm can be found in reports by Kaushik et al.^[39], and Yadav et al.^[40] 60,000 out of 70,000 MNIST dataset samples were used as the training data, and the remaining 10,000 samples were used for testing. Figure 4d shows that test accuracy when each synapse is modeled after the device experimental data, including its nonlinearity and asymmetry (Figure 4b), reaches 90.06 % within 5 epochs. Test accuracy numbers for the network 32-bit ideal synaptic weights and 6-bit quantized synaptic weights are 98.15 % and 91.5 % respectively. The on-chip inference test accuracy data, where synaptic weight updates are based on all the three pulse schemes described earlier, is tabulated in Table 2, supporting information 9. The energy consumption per spike ($E_{perspike}$) is 1.38 nJ for a -5 V gate voltage spike during potentiation and 16.8 nJ for a 5 V gate voltage spike during depression. $E_{perspike} = I_{PSC} * V_D * t_{spike}$, where I_{PSC} denotes the maximum postsynaptic current and t_{spike} denotes the pulse width of the presynaptic voltage spike.^[41]

The HT-MoS₂ FET also exhibits spike time-dependent plasticity (STDP),^[42] wherein synaptic strength depends upon the causal relationship between pre- and post-neuron firing.^[43] Synaptic efficacy gets potentiated (weakened) when the pre-neuron fires before (after)

the post-neuron in a few ms temporal gap. The time interval $\Delta t = t_{post} - t_{pre}$, between post- and pre-pulse occurrence, decides the weight update (ΔW),

$$\Delta W(\%) = 100 \times \frac{G_{after} - G_{before}}{G_{before}} \quad (1)$$

where G_{before} , and G_{after} denote the conductance values before and after one iteration of paired-pulse application separated by Δt . Figure 4e shows the measured STDP data for the HT-MoS₂ synapse for positive and negative 5 V pulses separated by varying Δt . Exponential fits (supporting information 10) for decrease and increase in synaptic strength for positive and negative Δt yield time constants of 113 ms and 337 ms, respectively. Unsupervised learning tested on Fisher’s iris dataset using a spiking neural network (SNN)^[44] based on this STDP data yields a stable test accuracy of 96.2 % after 2 epochs, as shown in Figure 4f.

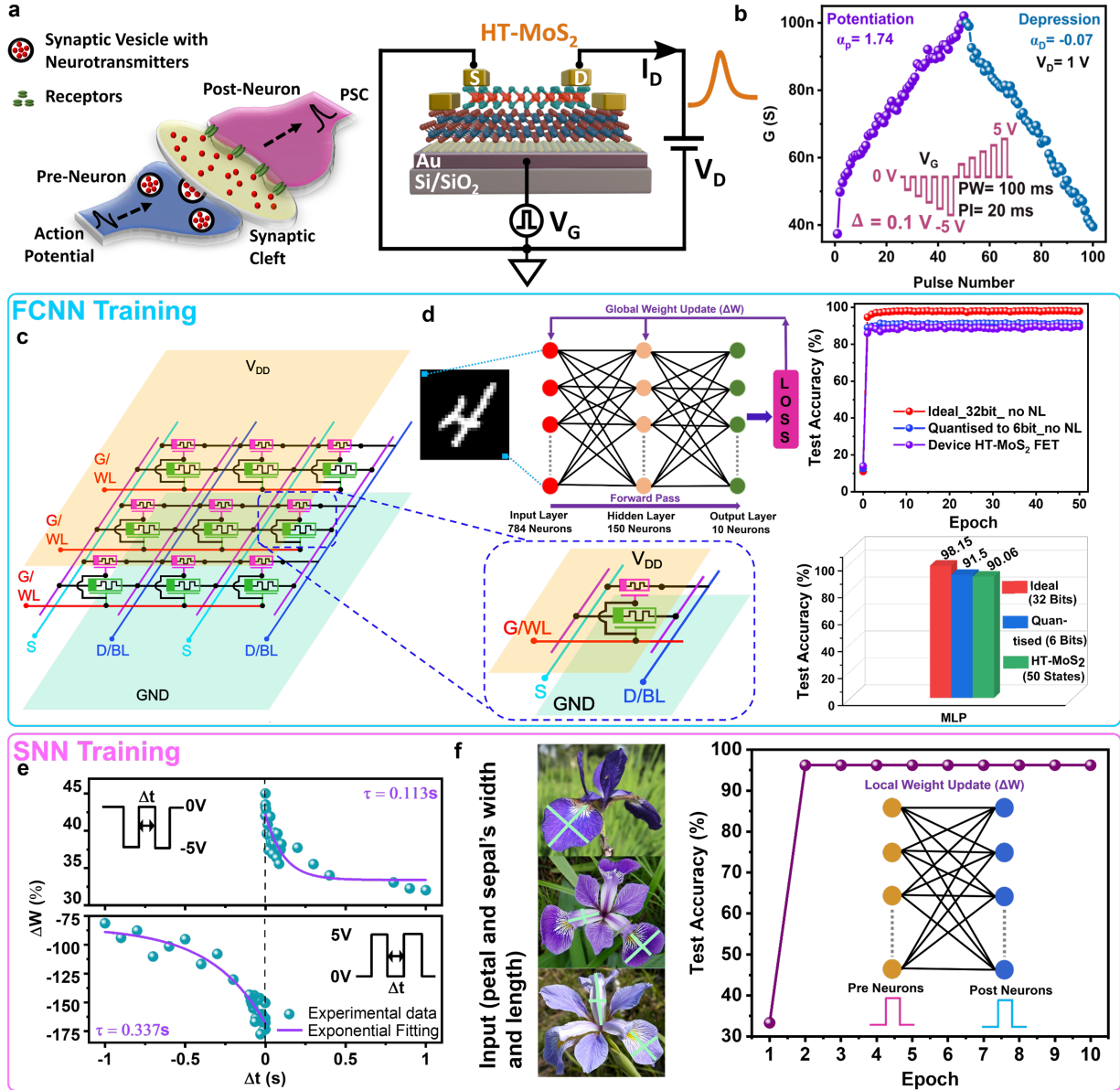


Figure 4: Neuromorphic in-memory computing using HT-MoS₂ synapse. (a) Biological synaptic junction equivalent electrical circuit for HT-MoS₂ FET under gate and source/drain biases. (b) Measured potentiation and depression characteristics of HT-MoS₂ synaptic FET. (c) 3D schematic of HT-MoS₂ FET integration in standard crossbar structure. (d) Fully connected neural network (FCNN) of non-spiking type trained to classify MNIST handwritten digits using a back-propagation algorithm with weight update limited to one potentiation/depression step at any iteration. Each input neuron corresponds to a unique pixel in the image. On-chip learning accuracy numbers (in data plot and bar chart) are shown for: synaptic weights with ideal 32-bit precision, with 6-bit precision without non-linearity, and those following the experimentally obtained potentiation and depression curves as shown in (b). (e) Measured STDP behavior of HT-MoS₂ synaptic FET. (f) Training accuracy of a spiking neural network (SNN) on Fisher's iris dataset, using experimental STDP data of (e) for weight update during training.^[45–47]

Heterosynaptic Plasticity and Synaptic Interactions: Extending the measurements done on the single synaptic HT-MoS₂ FET, the two vertically stacked synapses (HB-In₂Se₃ and HT-MoS₂) of the VSFET can be accessed simultaneously by biasing their S/D terminals, as shown in Figure 5a. The source and drain terminals of each channel layer (In₂Se₃ or MoS₂) represent the synaptic ends, and the channel itself represents the synaptic cleft. A single gate terminal simultaneously modulates the conductance of each synaptic channel, beyond the transverse local gate field, wherein, 1) it directly modulates the polarization bound charge and hence the free carrier accumulation and depletion at the hBN/In₂Se₃ interface of the HB-In₂Se₃ channel, and 2) it indirectly affects the carrier accumulation at the In₂Se₃/MoS₂ interface through the modulated polarization charge in the In₂Se₃ layer. This five-terminal measurement of heterosynaptic plasticity, where the plasticity in one input-specific synapse also triggers plasticity in another synapse^[48], unlike the plain positive feedback homosynaptic plasticity of the HT-MoS₂ FET alone, is more useful in maintaining synaptic weight stability, refining synaptic connections and balancing NNs.^[49,50]

Simultaneously measured $I_D - V_G$ curves for the HT-MoS₂ ($I_{DM} - V_G$, $V_{DM} = 1$ V) and HB-In₂Se₃ ($I_{DI} - V_G$, $V_{DI} = 1$ V) FETs are shown in Figure 5b, indicating clockwise hysteresis in both, similar to individually accessed FET characteristics. Further, the VSFET can demonstrate complex but fundamental biological functions such as synaptic cooperation and competition that favor in building and refinement of neural nets.^[51] Synaptic cooperation^[52,53] involves a group of synapses that work together and undergo a similar kind of plasticity change (P/D) in the neural circuit (Figure 5c). Applying incremental voltage stimuli at the gate terminal with $V_{DM} = 1$ V, $V_{DI} = 1$ V directly modulates the synaptic strength of the bottom HB-In₂Se₃ memtransistor, which also causes a similar synaptic plasticity response in the upper HT-MoS₂ memtransistor. Figure 5c shows the simultaneous measured P/D responses of the MoS₂ and In₂Se₃ synapses. Figure 5d shows three repeated cycles of P/D data for the two synapses where the MoS₂ synapse is stronger than In₂Se₃, indicating synaptic cooperation. While HT-MoS₂ shows a stronger synaptic connection than

HB-In₂Se₃ for all P/D cycles with $V_{DM} = 1$ V, $V_{DI} = 1$ V, changing V_{DI} to -1 V, keeping V_{DM} the same, makes the In₂Se₃ synapse stronger than MoS₂ as shown in Figure 5e, indicating synaptic competition. Repeating this over three P/D cycles, the HB-In₂Se₃ synaptic connection weakens and catches up with HT-MoS₂ conductance strength, demonstrating a biological habituation response (Figure 5f).

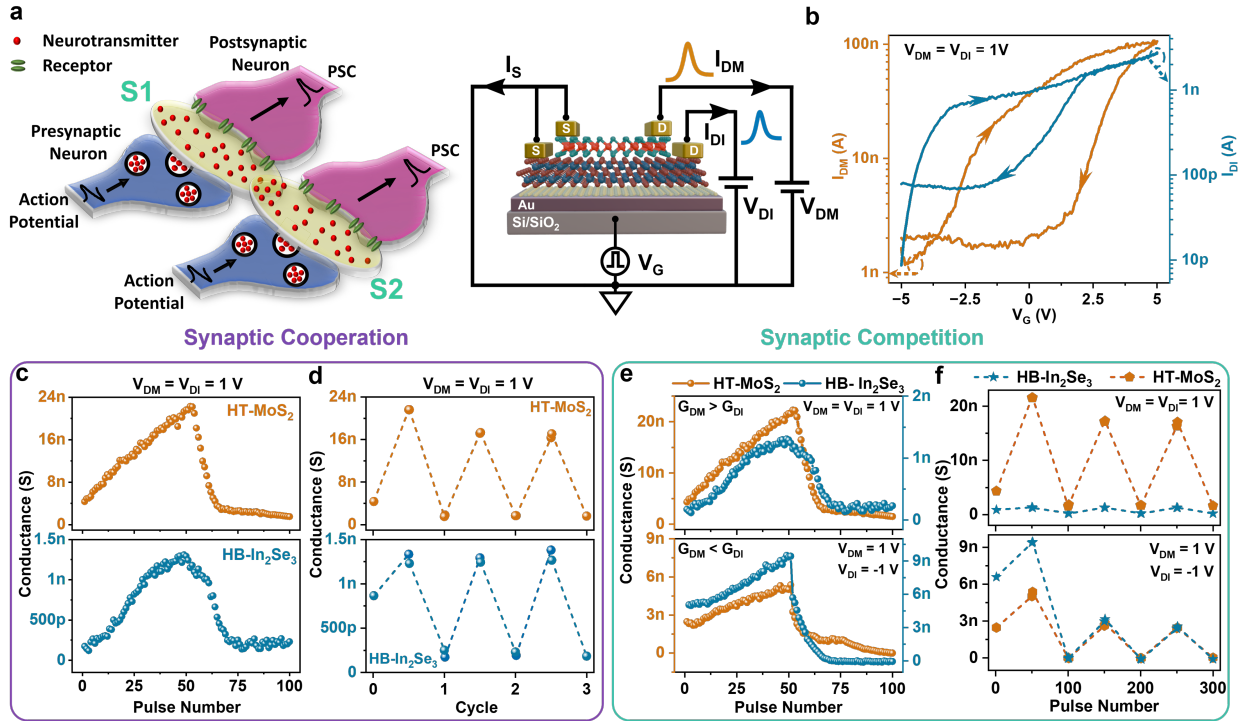


Figure 5: Heterosynaptic interactions utilizing VSFET. (a) Schematics showing two interacting biological synapses and their five-terminal equivalent electrical circuit representation using the VSFET. (b) Simultaneously extracted $I_D - V_G$ curves of HT-MoS₂ and HB-In₂Se₃ FETs under the biasing scheme shown in (a). Synaptic cooperation: (c) common gate pulsing causes similar potentiation (depression) behavior in HT-MoS₂ when HB-In₂Se₃ is potentiated (depressed), (d) multiple P/D cycles of synaptic cooperation between HT-MoS₂ and HB-In₂Se₃. Synaptic competition: (e) modifying V_{DI} from +1 V to -1 V flips the relative strengths of HT-MoS₂ and HB-In₂Se₃ synapses, leading to competitive behavior, (f) multiple P/D cycles of synaptic competition between HT-MoS₂ and HB-In₂Se₃ leading to eventual habituation.

Biomimetic Heterosynaptic Interactions in Sea Mollusk: Heterosynaptic interactions between the HT-MoS₂ and HB-MoS₂ synapses are shown to mimic the gill withdrawal reflex (GWR) action in *Aplysia californica*, a marine mollusk. *Aplysia*'s NN details are given

in supporting information 11. Figure 6a shows the VSFET electrical circuit where the two drain terminals V_{DM} and V_{DI} emulate sensory neurons 1 (SN1) and 2 (SN2), whose PSCs represent the sensory synaptic paths P_1 (SN1 \rightarrow MN) and P_2 (SN2 \rightarrow MN) to the motor neuron (MN). The gate terminal provides the modulatory stimulus to help the mollusk learn certain behaviors. The middle image of Figure 6a, where $V_{DM} = V_{DI} = 1$ V, shows a biological analogy to noxious stimuli at the tail and siphon of the mollusk, and the repetitive, pulsed V_G represents a modulatory signal for learning. Likewise, the bottom image in Figure 6a depicts the change in MN response when the stimulus changes for one sensory neuron ($V_{DI} = -1$ V), for the same input at SN1 and the same modulatory signal. Figure 6b shows cooperative synaptic interaction between P_1 and P_2 for harmful stimuli at the two SNs ($V_{DM} = V_{DI} = 1$ V). A small incremental change ($\Delta V_G = -0.1$ V) in the modulatory stimulus potentiates the synaptic strength in both sensory paths leading to MN response manifesting as gill contraction. Here, P_1 has stronger synaptic strength compared to P_2 , and hence, it makes a stronger contribution to MN response than P_2 . However, when the input to SN2 changes ($V_{DI} = -1$ V), P_2 becomes stronger than P_1 (Figure 6c), depicting competitive behavior. Here, the MN response is slightly weaker. Alternate cycles of cooperation and competition between P_1 and P_2 are shown in Figure 6c. Figure 6d shows how the electrical circuit mimics memory and learning behavior in the mollusk for small incremental $\Delta V_G = -0.1$ V. It first learns slowly how to react to small and incremental inputs ($\Delta V_G = -0.1$ V, $V_G = -0.1$ V to -2 V) such that when a strong aversive stimulus ($V_G = -5$ V) comes, it enhances its reflex action due to net synaptic strength enhancement. This refers to sensitization learning behavior in the mollusk, where a surge in neurotransmitter release by the SNs occurs at their synaptic clefts with MNs.^[54] This behavior emerges due to synaptic cooperation. For similar, continued, and redundant strong stimuli at the gate terminal ($V_G = -5$ V), the motor neuron response slope decreases, showing a decrease in the strength of synaptic connections. This refers to habituation, another form of synaptic competition. Hence, in summary, the gill reflex action of *Aplysia* mollusk can be efficiently trained through sensitization and habituation forms of

learning. [55]

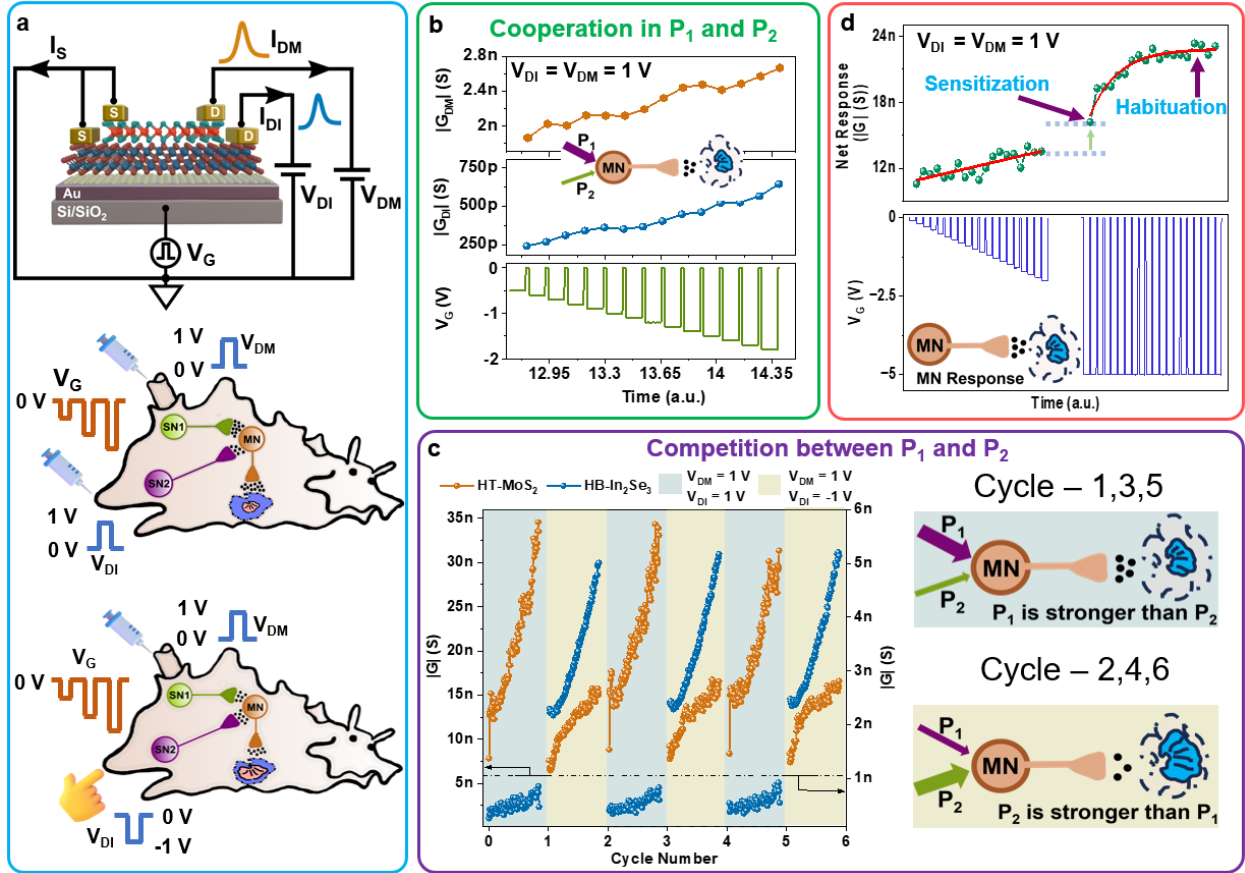


Figure 6: Biomimetic heterosynaptic response and defensive learning behavior of sea mollusk. (a) VSFET electrical circuit equivalence to biological dual-synaptic paths (P₁ and P₂) of Aplysia sea mollusk connecting its sensory neurons (SN1 and SN2) to the gill motor neuron (MN). The middle and bottom images show the siphon and tail of Aplysia getting stimulated by different tactile (electrical) stimuli. (b) Synaptic cooperative action between P₁ and P₂ leading to MN-actuated gill withdrawal response. (c) Alternate cycles of synaptic competition between P₁ and P₂ resulting in different MN gill responses. (d) Sensitization and habituation forms of learning and training of the gill reflex action to varying stimuli at the gate terminal.

Boolean Logic Gate Functionality: The VSFET can be easily re-configured to function as a 2-input NOT or NOR logic gate. Figure 7a shows the device biasing scheme and equivalent circuit for logic inputs x (V_G) and y (V_{DI}), where net source current (I_S) is the logic output and $V_{DM} = 1$ V. To realize the NOT gate, as shown in Figure 7b, a 0 V at x gives a high output current (output = 1), and 10 V at x gives a low output current (output = 0)

irrespective of the voltage applied at y . Likewise, Figure 7c shows NOR gate implementation where a 0 V signal applied at both x and y terminals ($x = y = 0$) results in high I_S (output = 1) while other combinations of 0 V and |10 V| at x and y give a low I_S (output = 0). In summary, VSFET can be reconfigured to realize complete Boolean logic.

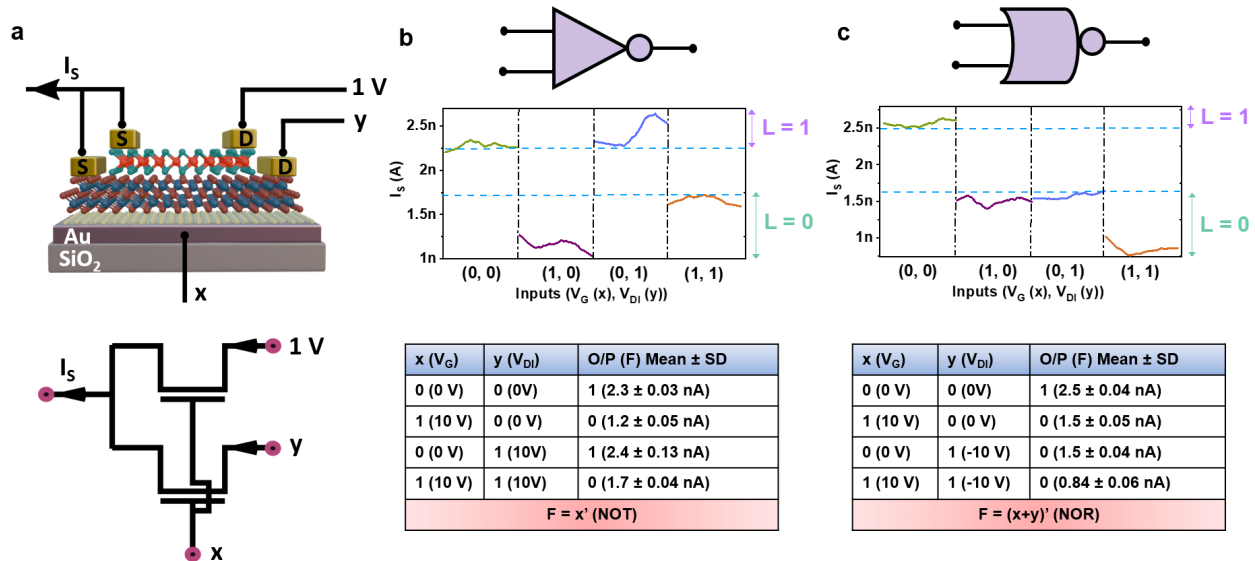


Figure 7: Boolean logic gates using VSFET. (a) 2D device cross-section biasing schematic and equivalent electrical circuit showing the two input variables x and y and the net source output current I_S . Output current under different input combinations and the corresponding truth table listing the signal and logic values for (b) NOT, and (c) NOR gate implementation using VSFET.

Conclusion

This work demonstrates a compact, multifunctional (logic and neuromorphic computing), and reconfigurable (logic \rightleftharpoons (multi) synaptic memory) VSFET. As shown in Table 1, previous reports of multifunctional and reconfigurable devices are based on trapping, filamentary, phase transition, defects, or electrostatic/ferroelectric gating. The VSFET, on the other hand, leverages the electrostatic coupling between a 2D non-ferroelectric semiconducting MoS₂ channel with a 2D ferroelectric semiconducting In₂Se₃ channel in a vertical heterostructure. Utilizing the out-of-plane In₂Se₃ ferroelectricity induced non-intrinsic gate-modulated hysteresis in the MoS₂ FET, we show homosynaptic plasticity enabled high supervised and

unsupervised learning accuracy in artificial and spiking NNs, respectively. Going one step further, simultaneous measurements of gate-controlled memtransistor behaviors of both, the In_2Se_3 (intrinsic) and the MoS_2 (non-intrinsic) channels allow the realization of complex heterosynaptic plasticity behaviors such as synaptic cooperation and competition where the maximum power consumption with both the transistors operational is as low as 6.85 nW at $V_D = 0.5$ V. These are shown to efficiently mimic the advanced sensorimotor NN controlling gill withdrawal reflex sensitization and habituation in a sea slug (*Aplysia*). The logic reconfigurability of the VSFET to realize Boolean gates, in addition to its area- and power-efficient multi-memory capabilities, offers significant design flexibility for advanced computing technologies.

Table 1: Summary of recently reported area- and energy-efficient reconfigurable devices for multifunctional neuromorphic computing.^[33,52,56–63] Here, device reconfigurability indicates easy transitions across the single synapse, multi-synapse and Boolean logic configurations utilizing the same device.

Material(s) Device Working Principle	Area Efficiency	Reconfigurability	Homosynaptic Plasticity						Heterosynaptic Interaction			
			P/D	Energy per spike (P/D)	NL α_p/α_d ($\alpha_p - \alpha_d$)	ANN Accuracy% Dataset Epoch	STDP	SNN Accuracy% Dataset Epoch	Plasticity	Coop./Comp.	Biometric	
WSe ₂ Split gates homojunction ^[56] Electrostatic control	Multi-device Vertical	Yes	×	×	×	×	×	✓	×	×	×	×
In ₂ Se ₃ Memristor ^[33] Ferroelectric (IP)	Lateral	Yes	✓	8 pJ/8 pJ	×	✓91 MNIST 30	✓	✓	✓89 grey pattern 30	✓	✓	×
MoS ₂ Memristor ^[57] Defect Motion (grain boundaries)	Vertical	No	✓	13.5 nJ/13.5 nJ	×	×	✓	✓	×	✓	×	×
TaO _x Memristor ^[58] Filamentary	Vertical	Yes	✓	120 pJ/186 pJ	×	✓	×	×	×	✓	×	×
TiO _{2-x} Memristor ^[59] Defect Motion (Vacancies)	Lateral	No	✓	6 mJ/6 mJ	×	×	✓	✓	×	✓	×	✓
Li _x MoO ₃ Memristor ^[60] Ion migration	Lateral	Yes	✓	×	×	×	×	×	×	✓	×	×
Li _x MoS ₂ Memristor ^[52] Phase Transition	Lateral	No	✓	8 nJ/8 nJ	×	×	×	×	×	✓	✓	×
WSe ₂ Memristor ^[61] Trapping	Vertical	No	✓	5.4 μ J/4.725 μ J	1/9.6 (-8.6)	×	×	×	×	✓	✓	✓
PVP Memristors ^[62] Filamentary	Vertical	No	✓	100 μ J/-	×	×	×	×	×	✓	×	×
Pentacene/APTES Memristor ^[63] Trapping	Vertical + Lateral	No	✓	1 μ J/675 pJ	×	✓96.42 MNIST 250	×	×	×	✓	✓	×
MoS ₂ /In ₂ Se ₃ Memristors Ferroelectric coupling (OOP) This Work	Vertically stratified transistors	Yes	✓	1.38 nJ/16.8 nJ	1.74/-0.07 (1.81)	✓90.06 MNIST 5	✓	✓	✓96.2 Fisher's Irish 2	✓	✓	✓

Experimental Procedure

Device Fabrication: Local-gate Au electrodes were first patterned on top of a p⁺ Si/SiO₂ (285 nm) substrate with the help of e-beam lithography (EBL, Raith 150-Two) followed by metal (Ti 4 nm/Au 30 nm) deposition (AJA sputter system) and lift-off. Single crystals of MoS₂ and In₂Se₃ were purchased from 2D semiconductors, and hBN crystals were purchased from SPI Supplies. An hBN flake was micromechanically exfoliated using adhesive scotch tape and transferred from the scotch tape to a polydimethylsiloxane (PDMS) stamp. The PDMS stamp was fixed onto a glass slide attached to a micromanipulator. The hBN flake was focus transferred on top of the prefabricated local-gate pattern using the micromanipulator under an Olympus BX-63 microscope. During the transfer process, the Si/SiO₂ substrate with the gate pattern was placed on top of a micro heater. After the hBN was aligned and placed on top of the gate pattern, the entire structure, consisting of the Si/SiO₂ substrate, the hBN flake along with the PDMS stamp, and the glass slide, was heated up to weaken the adhesion between the PDMS stamp and the hBN flake leaving behind only the hBN flake on top of the gate pattern after PDMS release. The same transfer process was followed for aligning and placing a thick (43.2 nm) In₂Se₃ flake on top of the hBN flake in the patterned gate area. Next, a rectangular (3.3 μm × 32.6 μm), thin (4.5 nm) MoS₂ flake was transferred on top of the In₂Se₃ and hBN flakes in such a way that a portion of the MoS₂ flake lay on the In₂Se₃/hBN overlap portion, and the rest on the hBN flake. The overlap portion of MoS₂ and In₂Se₃ flakes forms an MoS₂/In₂Se₃ vertical heterostructure, and the single portions of MoS₂ and In₂Se₃ flakes lying on hBN form the channel layers for control MoS₂ and In₂Se₃ FETs. Next, source/drain contacts were patterned using EBL on the MoS₂/In₂Se₃ heterostructure and the stand-alone In₂Se₃ and MoS₂ FETs. Finally, contact metallization (Ti 4 nm/Au 100 nm) and lift-off were carried out to complete the device fabrication.

Device Characterization: Electrical measurements were carried out in ambient conditions using a Keysight B1500A semiconductor device analyzer. The steady-state response was measured using Keysight B1500A's HRSMU and MPSMUs, and the pulsed response

was measured using Keysight B1500A's WGFMs.

Acknowledgement

The authors express their gratitude to the Indian Institute of Technology Bombay Nano Fabrication Facility (IITBNF) and the 2D Materials and Devices Lab for providing access to facilities for device fabrication and characterization. S.S. acknowledges the support of the Prime Minister's Research Fellowship (PMRF) PhD scheme, Government of India. S.L. acknowledges funding support from the Department of Science and Technology, under the project grant DST/NM/TUE/QM - 8/2019 (G)/2 and also from project grant FIR/2022/000005 of SERB, Government of India.

References

- [1] Thakar, K.; Rajendran, B.; Lodha, S. Ultra-low power neuromorphic obstacle detection using a two-dimensional materials-based subthreshold transistor. *npj 2D Materials and Applications* **2023**, *7*, 68.
- [2] Ajayan, J.; Mohankumar, P.; Nirmal, D.; Joseph, L. L.; Bhattacharya, S.; Sreejith, S.; Kollem, S.; Rebelli, S.; Tayal, S.; Mounika, B. Ferroelectric field effect transistors (FETs): advancements, challenges and exciting prospects for next generation non-volatile memory (NVM) applications. *Materials Today Communications* **2023**, *35*, 105591.
- [3] Lipatov, A.; Sharma, P.; Gruverman, A.; Sinitskii, A. Optoelectrical Molybdenum Disulfide (MoS₂)—Ferroelectric Memories. *ACS nano* **2015**, *9*, 8089–8098.
- [4] Tian, B.; Liu, L.; Yan, M.; Wang, J.; Zhao, Q.; Zhong, N.; Xiang, P.; Sun, L.; Peng, H.; Shen, H.; others A robust artificial synapse based on organic ferroelectric polymer. *Advanced Electronic Materials* **2019**, *5*, 1800600.

- [5] Chen, L.; Wang, L.; Peng, Y.; Feng, X.; Sarkar, S.; Li, S.; Li, B.; Liu, L.; Han, K.; Gong, X.; others A van der Waals synaptic transistor based on ferroelectric Hf_{0.5}Zr_{0.5}O₂ and 2D tungsten disulfide. *Advanced Electronic Materials* **2020**, *6*, 2000057.
- [6] Ram, A.; Maity, K.; Marchand, C.; Mahmoudi, A.; Kshirsagar, A. R.; Soliman, M.; Taniguchi, T.; Watanabe, K.; Doudin, B.; Ouerghi, A.; others Reconfigurable multifunctional van der Waals ferroelectric devices and logic circuits. *ACS nano* **2023**, *17*, 21865–21877.
- [7] Wang, W.; Meng, Y.; Wang, W.; Zhang, Y.; Li, B.; Yan, Y.; Gao, B.; Ho, J. C. 2D ferroelectric materials: Emerging paradigms for next-generation ferroelectronics. *Materials Today Electronics* **2023**, *6*, 100080.
- [8] Baek, S.; Yoo, H. H.; Ju, J. H.; Sriboriboon, P.; Singh, P.; Niu, J.; Park, J.-H.; Shin, C.; Kim, Y.; Lee, S. Ferroelectric field-effect-transistor integrated with ferroelectrics heterostructure. *Advanced Science* **2022**, *9*, 2200566.
- [9] Liu, F.; You, L.; Seyler, K. L.; Li, X.; Yu, P.; Lin, J.; Wang, X.; Zhou, J.; Wang, H.; He, H.; others Room-temperature ferroelectricity in CuInP₂S₆ ultrathin flakes. *Nature communications* **2016**, *7*, 1–6.
- [10] Wang, C.; You, L.; Cobden, D.; Wang, J. Towards two-dimensional van der Waals ferroelectrics. *Nature Materials* **2023**, *22*, 542–552.
- [11] Ghosh, S.; Varghese, A.; Jawa, H.; Yin, Y.; Medhekar, N. V.; Lodha, S. Polarity-tunable photocurrent through band alignment engineering in a high-speed WSe₂/SnSe₂ diode with large negative responsivity. *ACS nano* **2022**, *16*, 4578–4587.
- [12] Varghese, A.; Saha, D.; Thakar, K.; Jindal, V.; Ghosh, S.; Medhekar, N. V.; Ghosh, S.; Lodha, S. Near-direct bandgap WSe₂/ReS₂ type-II pn heterojunction for enhanced ultrafast photodetection and high-performance photovoltaics. *Nano letters* **2020**, *20*, 1707–1717.

- [13] Belianinov, A.; He, Q.; Dziaugys, A.; Maksymovych, P.; Eliseev, E.; Borisevich, A.; Morozovska, A.; Banyas, J.; Vysochanskii, Y.; Kalinin, S. V. CuInP2S6 room temperature layered ferroelectric. *Nano letters* **2015**, *15*, 3808–3814.
- [14] Si, M.; Saha, A. K.; Gao, S.; Qiu, G.; Qin, J.; Duan, Y.; Jian, J.; Niu, C.; Wang, H.; Wu, W.; others A ferroelectric semiconductor field-effect transistor. *Nature Electronics* **2019**, *2*, 580–586.
- [15] Liao, J.; Wen, W.; Wu, J.; Zhou, Y.; Hussain, S.; Hu, H.; Li, J.; Liaqat, A.; Zhu, H.; Jiao, L.; others Van der Waals ferroelectric semiconductor field effect transistor for in-memory computing. *ACS nano* **2023**, *17*, 6095–6102.
- [16] Chang, K.; Küster, F.; Miller, B. J.; Ji, J.-R.; Zhang, J.-L.; Sessi, P.; Barraza-Lopez, S.; Parkin, S. S. Microscopic manipulation of ferroelectric domains in SnSe monolayers at room temperature. *Nano letters* **2020**, *20*, 6590–6597.
- [17] Higashitarumizu, N.; Kawamoto, H.; Lee, C.-J.; Lin, B.-H.; Chu, F.-H.; Yonemori, I.; Nishimura, T.; Wakabayashi, K.; Chang, W.-H.; Nagashio, K. Purely in-plane ferroelectricity in monolayer SnS at room temperature. *Nature communications* **2020**, *11*, 2428.
- [18] Bao, Y.; Song, P.; Liu, Y.; Chen, Z.; Zhu, M.; Abdelwahab, I.; Su, J.; Fu, W.; Chi, X.; Yu, W.; others Gate-tunable in-plane ferroelectricity in few-layer SnS. *Nano letters* **2019**, *19*, 5109–5117.
- [19] Xiao, J.; Zhu, H.; Wang, Y.; Feng, W.; Hu, Y.; Dasgupta, A.; Han, Y.; Wang, Y.; Muller, D. A.; Martin, L. W.; others Intrinsic two-dimensional ferroelectricity with dipole locking. *Physical review letters* **2018**, *120*, 227601.
- [20] Cui, C.; Hu, W.-J.; Yan, X.; Addiego, C.; Gao, W.; Wang, Y.; Wang, Z.; Li, L.; Cheng, Y.; Li, P.; others Intercorrelated in-plane and out-of-plane ferroelectricity in

- ultrathin two-dimensional layered semiconductor In₂Se₃. *Nano letters* **2018**, *18*, 1253–1258.
- [21] Park, S.; Lee, D.; Kang, J.; Choi, H.; Park, J.-H. Laterally gated ferroelectric field effect transistor (LG-FeFET) using α -In₂Se₃ for stacked in-memory computing array. *Nature Communications* **2023**, *14*, 6778.
- [22] Wang, S.; Liu, L.; Gan, L.; Chen, H.; Hou, X.; Ding, Y.; Ma, S.; Zhang, D. W.; Zhou, P. Two-dimensional ferroelectric channel transistors integrating ultra-fast memory and neural computing. *Nature Communications* **2021**, *12*, 53.
- [23] Kang, S.-J.; Jung, W.; Gwon, O. H.; Kim, H. S.; Byun, H. R.; Kim, J. Y.; Jang, S. G.; Shin, B.; Kwon, O.; Cho, B.; others Photo-Assisted Ferroelectric Domain Control for α -In₂Se₃ Artificial Synapses Inspired by Spontaneous Internal Electric Fields. *Small* **2024**, *20*, 2307346.
- [24] Kaushik, N.; Nipane, A.; Basheer, F.; Dubey, S.; Grover, S.; Deshmukh, M. M.; Lodha, S. Schottky barrier heights for Au and Pd contacts to MoS₂. *Applied Physics Letters* **2014**, *105*.
- [25] Jawa, H.; Varghese, A.; Ghosh, S.; Sahoo, S.; Yin, Y.; Medhekar, N. V.; Lodha, S. Wavelength-controlled photocurrent polarity switching in BP-MoS₂ heterostructure. *Advanced Functional Materials* **2022**, *32*, 2112696.
- [26] Yuan, P.; Li, C.; Xu, S.; Liu, J.; Wang, X. Interfacial thermal conductance between few to tens of layered-MoS₂ and c-Si: Effect of MoS₂ thickness. *Acta Materialia* **2017**, *122*, 152–165.
- [27] Lee, C.; Yan, H.; Brus, L. E.; Heinz, T. F.; Hone, J.; Ryu, S. Anomalous lattice vibrations of single-and few-layer MoS₂. *ACS nano* **2010**, *4*, 2695–2700.

- [28] Liu, K.; Zhang, T.; Dang, B.; Bao, L.; Xu, L.; Cheng, C.; Yang, Z.; Huang, R.; Yang, Y. An optoelectronic synapse based on α -In₂Se₃ with controllable temporal dynamics for multimode and multiscale reservoir computing. *Nature Electronics* **2022**, *5*, 761–773.
- [29] Dutta, D.; Mukherjee, S.; Uzhansky, M.; Koren, E. Cross-field optoelectronic modulation via inter-coupled ferroelectricity in 2D In₂Se₃. *npj 2D Materials and Applications* **2021**, *5*, 81.
- [30] Xue, F.; Zhang, J.; Hu, W.; Hsu, W.-T.; Han, A.; Leung, S.-F.; Huang, J.-K.; Wan, Y.; Liu, S.; Zhang, J.; others Multidirection piezoelectricity in mono-and multilayered hexagonal α -In₂Se₃. *ACS nano* **2018**, *12*, 4976–4983.
- [31] Wang, L.; Wang, X.; Zhang, Y.; Li, R.; Ma, T.; Leng, K.; Chen, Z.; Abdelwahab, I.; Loh, K. P. Exploring ferroelectric switching in α -In₂Se₃ for neuromorphic computing. *Advanced Functional Materials* **2020**, *30*, 2004609.
- [32] Varghese, A.; Pandey, A. H.; Sharma, P.; Yin, Y.; Medhekar, N. V.; Lodha, S. Electrically Controlled High Sensitivity Strain Modulation in MoS₂ Field-Effect Transistors via a Piezoelectric Thin Film on Silicon Substrates. *Nano Letters* **2024**, *24*, 8472–8480.
- [33] Xue, F.; He, X.; Wang, Z.; Retamal, J. R. D.; Chai, Z.; Jing, L.; Zhang, C.; Fang, H.; Chai, Y.; Jiang, T.; others Giant ferroelectric resistance switching controlled by a modulatory terminal for low-power neuromorphic in-memory computing. *Advanced Materials* **2021**, *33*, 2008709.
- [34] Jawa, H.; Varghese, A.; Lodha, S. Electrically tunable room temperature hysteresis crossover in underlap MoS₂ field-effect transistors. *ACS Applied Materials & Interfaces* **2021**, *13*, 9186–9194.
- [35] Mu, Y.; Yang, J.; Xie, G.; Wang, Z.; Guo, B.; Gong, J. R. Homo-type α -In₂Se₃/PdSe₂ Ferroelectric van der Waals Heterojunction Photodetectors with High-performance and Broadband. *Advanced Functional Materials* **2024**, 2315543.

- [36] Lyu, F.; Sun, Y.; Yang, Q.; Tang, B.; Li, M.; Li, Z.; Sun, M.; Gao, P.; Ye, L.-H.; Chen, Q. Thickness-dependent band gap of α -In₂Se₃: from electron energy loss spectroscopy to density functional theory calculations. *Nanotechnology* **2020**, *31*, 315711.
- [37] Elias, C.; Valvin, P.; Pelini, T.; Summerfield, A.; Mellor, C.; Cheng, T.; Eaves, L.; Foxon, C.; Beton, P.; Novikov, S.; others Direct band-gap crossover in epitaxial monolayer boron nitride. *Nature communications* **2019**, *10*, 2639.
- [38] Cassabois, G.; Valvin, P.; Gil, B. Hexagonal boron nitride is an indirect bandgap semiconductor. *Nature photonics* **2016**, *10*, 262–266.
- [39] Kaushik, D.; Sharda, J.; Bhowmik, D. Synapse cell optimization and back-propagation algorithm implementation in a domain wall synapse based crossbar neural network for scalable on-chip learning. *Nanotechnology* **2020**, *31*, 364004.
- [40] Yadav, R. S.; Gupta, P.; Holla, A.; Ali Khan, K. I.; Muduli, P. K.; Bhowmik, D. Demonstration of Synaptic Behavior in a Heavy-Metal-Ferromagnetic-Metal-Oxide-Heterostructure-Based Spintronic Device for On-Chip Learning in Crossbar-Array-Based Neural Networks. *ACS Applied Electronic Materials* **2023**, *5*, 484–497.
- [41] Hwang, Y.; Park, B.; Hwang, S.; Choi, S.-W.; Kim, H. S.; Kim, A. R.; Choi, J. W.; Yoon, J.; Kwon, J.-D.; Kim, Y. A Bioinspired Ultra Flexible Artificial van der Waals 2D-MoS₂ Channel/LiSiOx Solid Electrolyte Synapse Arrays via Laser-Lift Off Process for Wearable Adaptive Neuromorphic Computing. *Small Methods* **2023**, *7*, 2201719.
- [42] Crair, M.; Shah, R. Long-term potentiation and long-term depression in experience-dependent plasticity. **2009**,
- [43] Gütig, R. To spike, or when to spike? *Current opinion in neurobiology* **2014**, *25*, 134–139.

- [44] Sahu, U.; Pandey, A.; Goyal, K.; Bhowmik, D. Spike time dependent plasticity (STDP) enabled learning in spiking neural networks using domain wall based synapses and neurons. *AIP Advances* **2019**, *9*.
- [45] Stang, D. J. Iris setosa 2. https://commons.wikimedia.org/wiki/File:Iris_setosa_2.jpg, 2010; Accessed: 2024-07-01.
- [46] Mayfield, F. Iris versicolor 3. https://commons.wikimedia.org/wiki/File:Iris_versicolor_3.jpg, 2007; Accessed: 2024-07-01.
- [47] Richards, F. D. Iris virginica. https://commons.wikimedia.org/wiki/File:Iris_virginica.jpg, 2009; Accessed: 2024-07-01.
- [48] Chistiakova, M.; Bannon, N. M.; Bazhenov, M.; Volgushev, M. Heterosynaptic plasticity: multiple mechanisms and multiple roles. *The Neuroscientist* **2014**, *20*, 483–498.
- [49] Chistiakova, M.; Volgushev, M. Heterosynaptic plasticity in the neocortex. *Experimental brain research* **2009**, *199*, 377–390.
- [50] Jenks, K. R.; Tsimring, K.; Ip, J. P. K.; Zepeda, J. C.; Sur, M. Heterosynaptic plasticity and the experience-dependent refinement of developing neuronal circuits. *Frontiers in neural circuits* **2021**, *15*, 803401.
- [51] Ramiro-Cortés, Y.; Hobbiss, A. F.; Israely, I. Synaptic competition in structural plasticity and cognitive function. *Philosophical Transactions of the Royal Society B: Biological Sciences* **2014**, *369*, 20130157.
- [52] Zhu, X.; Li, D.; Liang, X.; Lu, W. D. Ionic modulation and ionic coupling effects in MoS₂ devices for neuromorphic computing. *Nature materials* **2019**, *18*, 141–148.
- [53] Miller, K. D. Synaptic economics: competition and cooperation in synaptic plasticity. *Neuron* **1996**, *17*, 371–374.

- [54] Castellucci, V.; Kandel, E. R. Presynaptic facilitation as a mechanism for behavioral sensitization in *Aplysia*. *Science* **1976**, *194*, 1176–1178.
- [55] Kandel, E. R. The molecular biology of memory storage: a dialogue between genes and synapses. *Science* **2001**, *294*, 1030–1038.
- [56] Pan, C.; Wang, C.-Y.; Liang, S.-J.; Wang, Y.; Cao, T.; Wang, P.; Wang, C.; Wang, S.; Cheng, B.; Gao, A.; others Reconfigurable logic and neuromorphic circuits based on electrically tunable two-dimensional homojunctions. *Nature Electronics* **2020**, *3*, 383–390.
- [57] Sangwan, V. K.; Lee, H.-S.; Bergeron, H.; Balla, I.; Beck, M. E.; Chen, K.-S.; Hersam, M. C. Multi-terminal memtransistors from polycrystalline monolayer molybdenum disulfide. *Nature* **2018**, *554*, 500–504.
- [58] Yang, Y.; Yin, M.; Yu, Z.; Wang, Z.; Zhang, T.; Cai, Y.; Lu, W. D.; Huang, R. Multifunctional Nanoionic Devices Enabling Simultaneous Heterosynaptic Plasticity and Efficient In-Memory Boolean Logic. *Advanced Electronic Materials* **2017**, *3*, 1700032.
- [59] Miyake, R.; Nagata, Z.; Adachi, K.; Hayashi, Y.; Tohei, T.; Sakai, A. Versatile functionality of four-terminal $\text{TiO}_2\text{-x}$ memristive devices as artificial synapses for neuromorphic computing. *ACS Applied Electronic Materials* **2022**, *4*, 2326–2336.
- [60] Qin, J.-K.; Zhu, B.-X.; Wang, C.; Zhu, C.-Y.; Sun, R.-Y.; Zhen, L.; Chai, Y.; Xu, C.-Y. Heterosynaptic plasticity achieved by highly anisotropic ionic migration in layered $\text{Li}_x\text{-MoO}_3$ for neuromorphic application. *Advanced Electronic Materials* **2022**, *8*, 2200721.
- [61] Ding, G.; Yang, B.; Chen, R.-S.; Mo, W.-A.; Zhou, K.; Liu, Y.; Shang, G.; Zhai, Y.; Han, S.-T.; Zhou, Y. Reconfigurable 2D WSe_2 -based memtransistor for mimicking homosynaptic and heterosynaptic plasticity. *Small* **2021**, *17*, 2103175.

- [62] Milano, G.; Pedretti, G.; Fretto, M.; Boarino, L.; Benfenati, F.; Ielmini, D.; Valov, I.; Ricciardi, C. Brain-inspired structural plasticity through reweighting and rewiring in multi-terminal self-organizing memristive nanowire networks. *Advanced Intelligent Systems* **2020**, *2*, 2000096.
- [63] Zheng, C.; Liao, Y.; Xiong, Z.; Zhou, Y.; Han, S.-T. Mimicking the competitive and cooperative behaviors with multi-terminal synaptic memtransistors. *Journal of Materials Chemistry C* **2020**, *8*, 6063–6071.

Vertically Integrated Dual-memtransistor Enabled Reconfigurable Heterosynaptic Sensorimotor Networks and In-memory Neuromorphic Computing Supporting Information

Srilagna Sahoo,[†] Abin Varghese,[‡] Aniket Sadashiva,[†] Mayank Goyal,[†] Jayatika
Sakhuja,[†] Debanjan Bhowmik,[†] and Saurabh Lodha^{*,†,¶}

[†]*Department of Electrical Engineering, Indian Institute of Technology Bombay, Mumbai
400076, India*

[‡]*Department of Engineering, King's College London, London WC2R 2LS, UK*

[¶]<https://orcid.org/0000-0002-0690-3169>

E-mail: slodha@ee.iitb.ac.in

Supporting Information 1: 2D cross-sections of C-MoS₂ and C-In₂Se₃ FETs and PFM characterization.

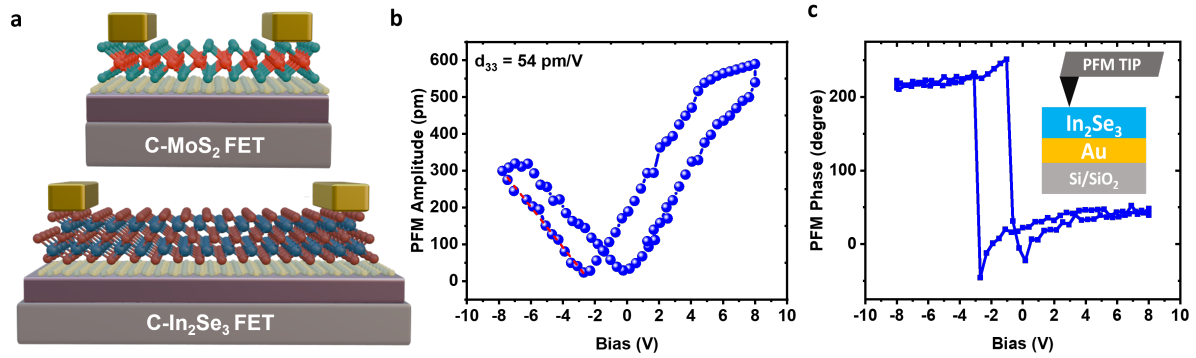


Figure S1: (a) 2D cross-sections of control MoS₂ FET (C-MoS₂ FET) and control In₂Se₃ FET (C-In₂Se₃ FET). Piezoresponse force microscopy (PFM) characterization of In₂Se₃ flake showing (b) PFM amplitude, and (c) PFM phase versus voltage hysteresis loop indicating clear ferroelectric polarization switching under an external electric field. The inset shows the schematic of the PFM measurement.

Supporting Information 2: Double sweep transfer ($I_D - V_G$) characteristics at $V_D = 1$ V and extracted memory window (MW)/sweep range (SR) ratios of two additional HT-MoS₂ FETs at $V_D = 1$ V.

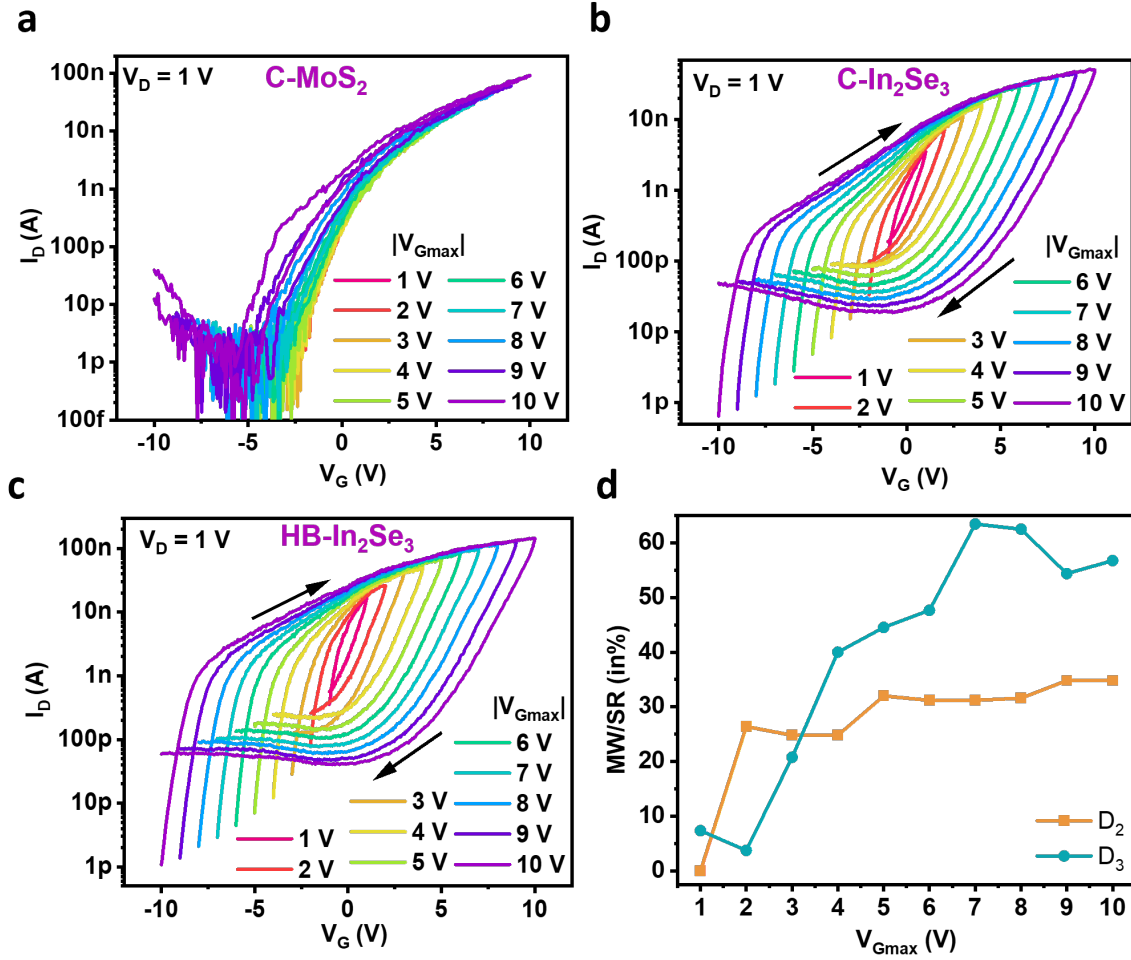


Figure S2: Double sweep transfer ($I_D - V_G$) characteristics of (a) C-MoS₂ FET, (b) C-In₂Se₃ FET, and (c) HB-In₂Se₃ FET for different maximum gate bias values. (d) MW/SR ratios extracted as a function of gate bias sweep range of two additional HT-MoS₂ FETs at $V_D = 1$ V.

Supporting Information 3: Double sweep transfer ($I_D - V_G$) characteristics and the extracted MW/SR ratios at $V_D = 0.5$ V.

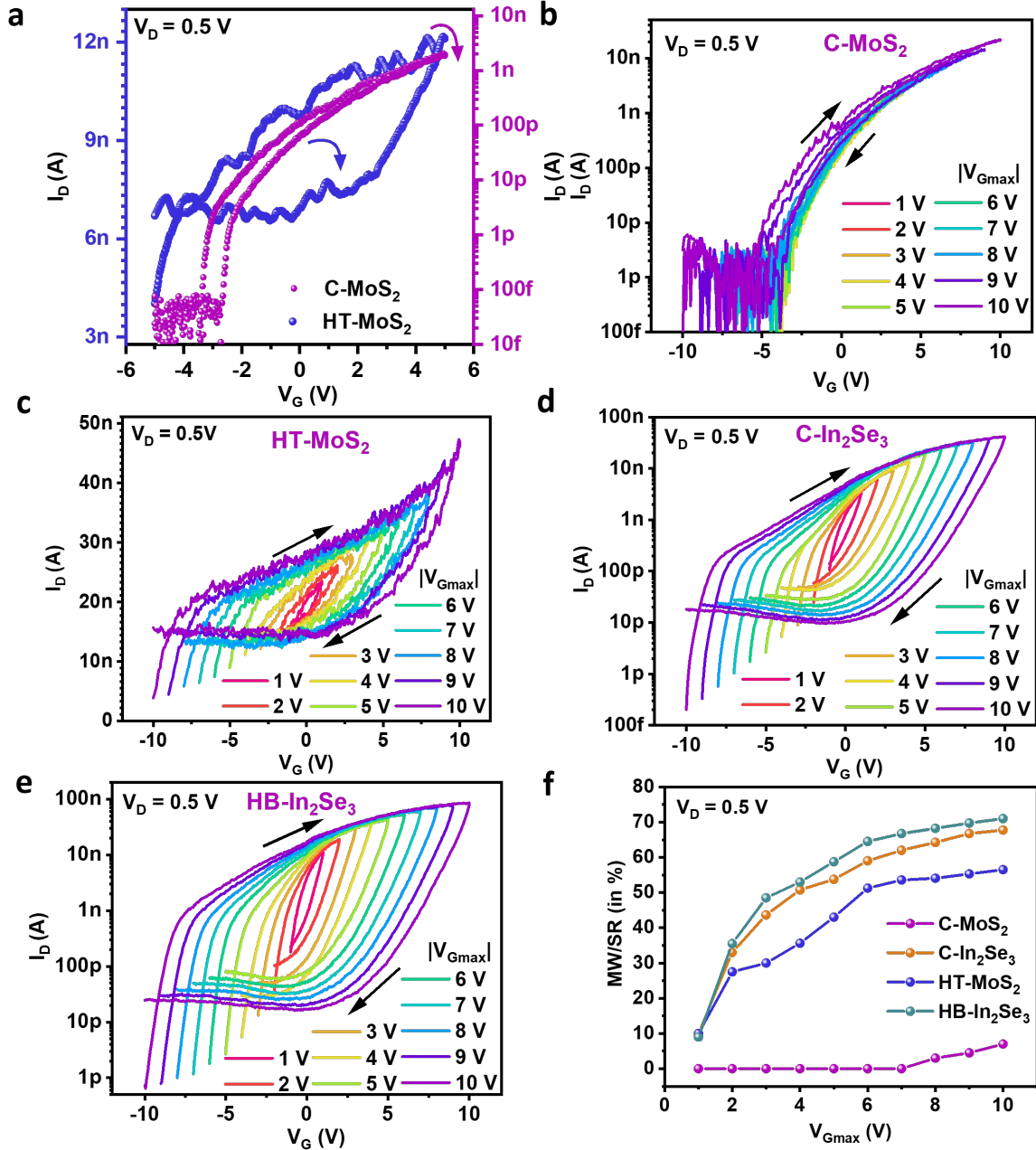


Figure S3: (a) Comparison of $I_D - V_G$ characteristics between C-MoS₂ and HT-MoS₂ FETs at $V_D = 0.5$ V. $I_D - V_G$ characteristics of (b) C-MoS₂, (c) HT-MoS₂, (d) C-In₂Se₃, and (e) HB-In₂Se₃ FETs for different maximum gate bias values at $V_D = 0.5$ V. (f) MW/SR ratios extracted as a function of gate bias sweep range from (b-e) at $V_D = 0.5$ V.

Supporting Information 4: Output ($I_D - V_D$) characteristics.

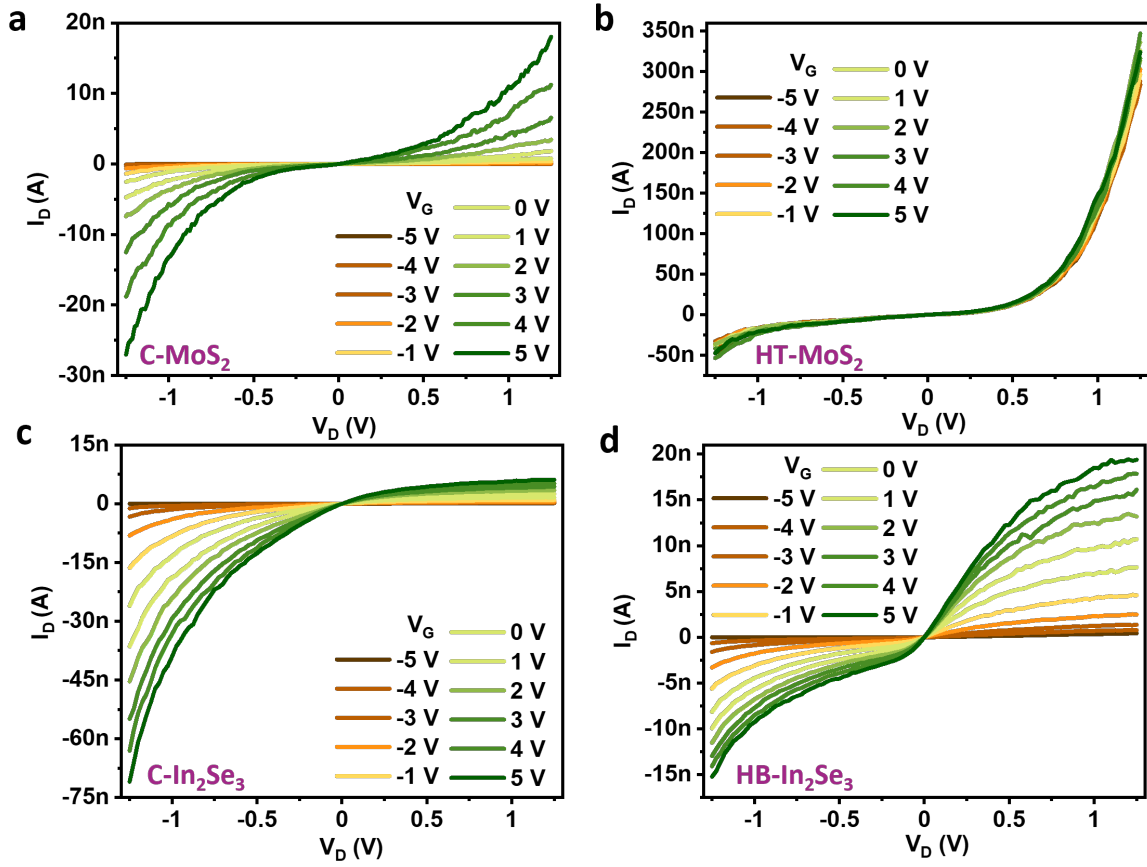


Figure S4: Output ($I_D - V_D$) characteristics of (a) C-MoS₂, (b) HT-MoS₂, (c) C-In₂Se₃, and, (d) HB-In₂Se₃ FETs for different gate bias values.

Supporting Information 5: Electron energy band diagrams.

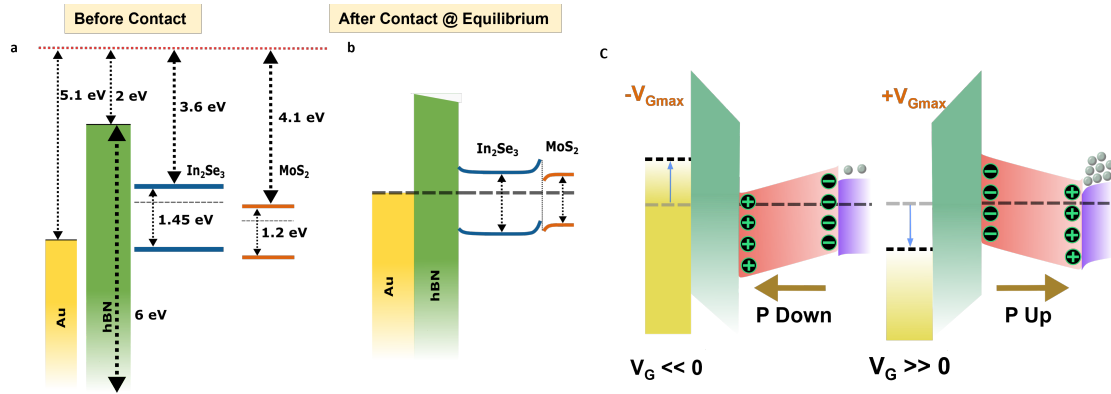


Figure S5: Electron energy band diagrams along Au/hBN//In₂Se₃/MoS₂ stack (a) before contact, (b) after contact at equilibrium, and, (c) at $-V_{Gmax}$ ($+V_{Gmax}$) indicating high negative (positive) gate field-induced strong downward (upward) In₂Se₃ polarization.

Supporting Information 6: Homosynaptic characteristics of HT-MoS₂ FET.

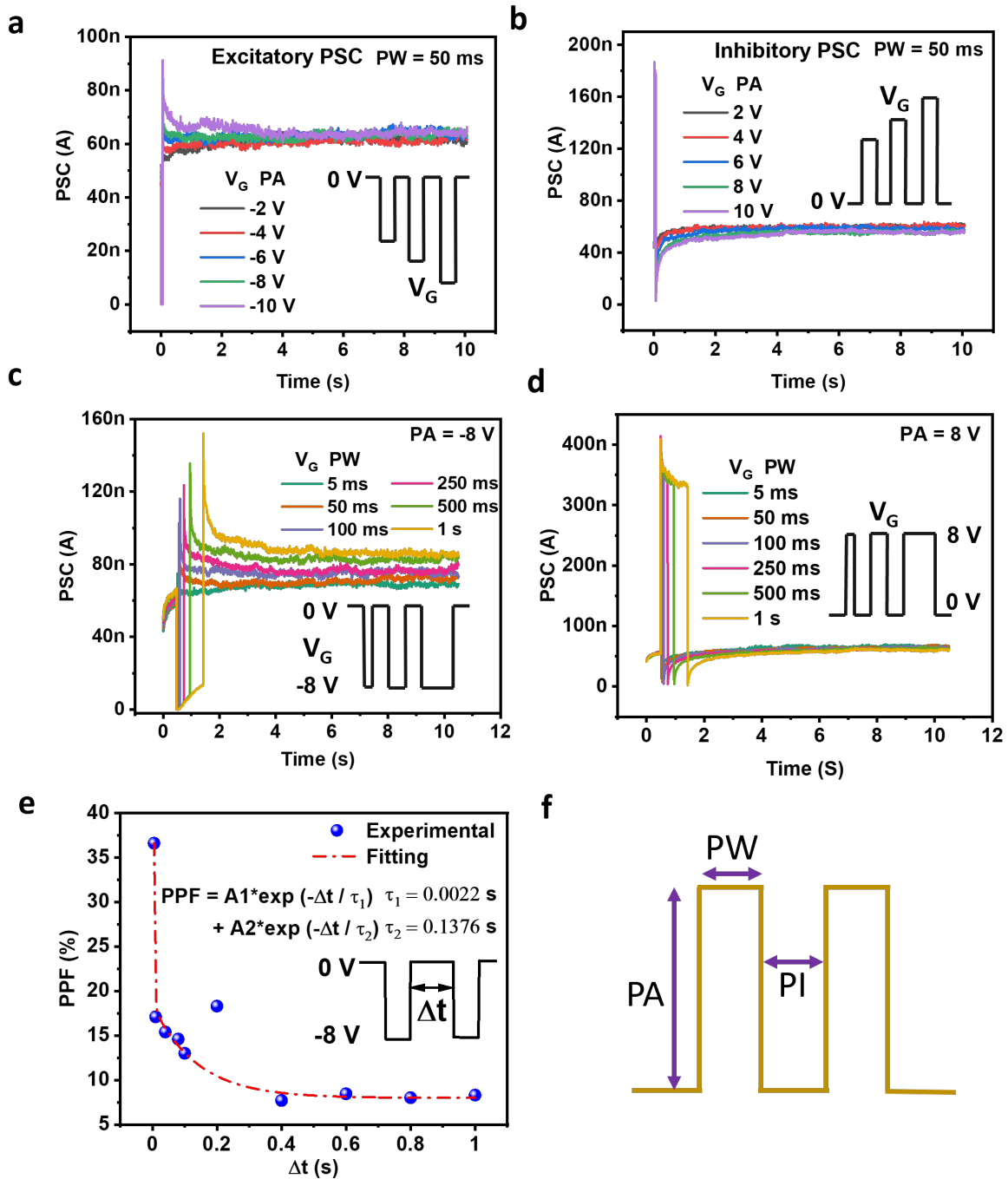


Figure S6: The postsynaptic current of HT-MoS₂ FET versus time for a single gate pulse of different pulse amplitudes (PAs): (a) $-V_G$, (b) $+V_G$ and different pulse widths (PWs) at (c) $V_G = -8$ V, and (d) $V_G = 8$ V at $V_D = 1$ V. (e) Paired pulse facilitation (PPF) versus pulse intervals (PIs), Δt , for pulse amplitude (PA) of $V_G = -8$ V and pulse width (PW) = 5 ms at $V_D = 1$ V. (f) Definition of PA, PW, and PI.

Supporting Information 7: P/D nonlinearity factor calculation.

The equations used for the nonlinearity factor calculations are as follows:

$$G_P = G_{\min} + \left((G_{\max} - G_{\min}) \cdot \left(1 - \exp\left(\frac{-n}{A_P}\right) \right) \right) \cdot \left(\frac{1}{1 - \exp\left(\frac{-1}{A_P}\right)} \right) \quad (\text{S1})$$

$$G_D = G_{\max} - \left((G_{\max} - G_{\min}) \cdot \left(1 - \exp\left(\frac{1-n}{A_D}\right) \right) \right) \cdot \left(\frac{1}{1 - \exp\left(\frac{1}{A_D}\right)} \right) \quad (\text{S2})$$

where $n = \text{pulse number}/n_{\max}$, $n_{\max} = N-1$, N is the total number of pulses, and G_{\max} and G_{\min} denote the normalized maximum and minimum conductance levels. The nonlinearity factors, α_p and α_d , are calculated by mapping A_P and A_D using DNN+Neurosim document.^[1]

Supporting Information 8: Additional P/D measurements of homosynaptic HT-MoS₂ FET.

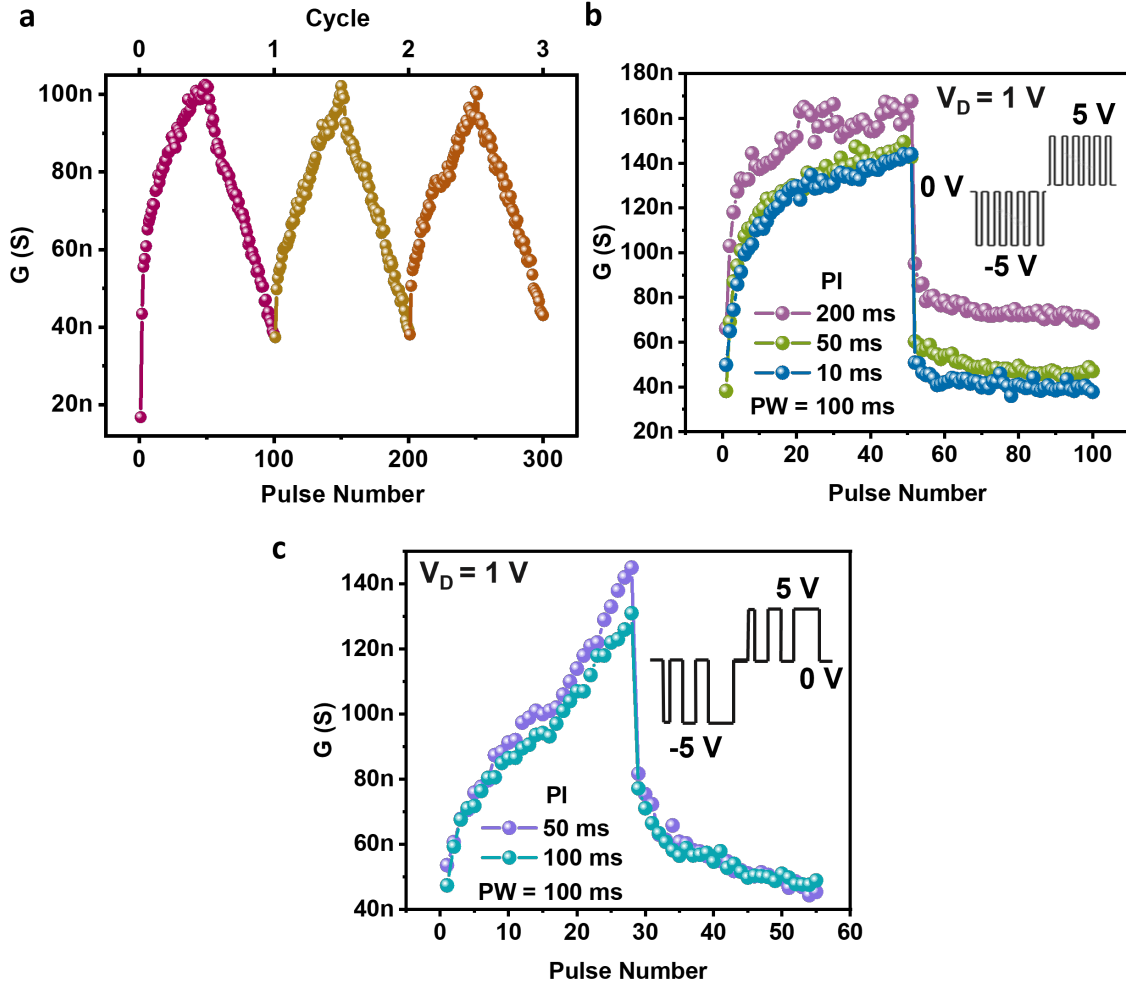


Figure S8: Potentiation/depression (P/D) curves of HT-MoS₂ FET under different pulse schemes. P/D curves vs pulse number for (a) multiple cycles of incremental amplitude pulse scheme, (b) identical pulse scheme at a fixed PW = 100 ms for different PIs, and (c) varied pulse-width scheme for different PIs at a drain voltage of 1 V.

Table 1: Nonlinearity factors evaluated from P/D curve versus pulse number of HT-MoS₂ FET for different pulse schemes.

Pulse Scheme	α_p	α_d
Identical	5.65	-
Incremental Amplitude	1.74	-0.07
Varied Pulse-width	0.74	-7.65

Supporting Information 9: Test accuracy for MNIST dataset on-chip inference (HT-MoS₂ synapse).

Table 2: Test accuracy values evaluated using MNIST dataset for on-chip inference utilizing a fully connected neural network (FCNN) for HT-MoS₂ FET.

Pulse Scheme	Test Accuracy (%)
Identical	97.08
Incremental Amplitude	97.21
Varied Pulse-width	97.2

Supporting Information 10: STDP data modeling (HT-MoS₂ synapse).

The exponential fitting equations used for the STDP curves are given by:

$$Y = Y_0 + A1*\exp(-\Delta t/ \tau) \text{ for } \Delta t > 0$$

$$Y = -Y_0 - A1*\exp(-\Delta t/ (-\tau)) \text{ for } \Delta t < 0$$

Y_0 denotes the residue, but with longer Δt , Y_0 is considered to be 0.

Supporting Information 11: Sensorimotor NN of sea mollusk (Aplysia).

Aplysia is a tiny sea mollusk with simple neural network containing only 10000 neurons.^[2] The gill withdrawal reflex (GWR) action in Aplysia is regulated by its sensorimotor neural network. This behavioral response can be extended to broader contexts, such as understanding learning and memory in human neural networks and creating therapeutic strategies for neurological disorders.

GWR action in the mollusk gets triggered when the tail or siphon (which has sensory neurons (SN)) gets stimulated by an external event which in turn triggers the modulatory interneuron (MIN). In response to the external stimulus, MIN releases serotonin, which triggers synaptic plasticity in the motor neurons (MN), leading to retraction/withdrawal of the gill.^[3,4]

References

- [1] Contributors, N. DNN NeuroSim V2.0 Nonlinearity Norms Documentation. https://github.com/neurosim/DNN_NeuroSim_V2.0/blob/master/Documents/Nonlinearity-NormA.htm, 2024; Accessed: 26 July 2024.
- [2] Moroz, L. L. Aplysia. *Current Biology* **2011**, *21*, R60–R61.
- [3] Pinsker, H.; Kupfermann, I.; Castellucci, V.; Kandel, E. Habituation and dishabituation of the gill-withdrawal reflex in Aplysia. *Science* **1970**, *167*, 1740–1742.
- [4] Chitwood, R. A.; Li, Q.; Glanzman, D. L. Serotonin facilitates AMPA-type responses in isolated siphon motor neurons of Aplysia in culture. *The Journal of physiology* **2001**, *534*, 501.